Convectively Coupled Equatorial Waves: Analysis of Clouds and Temperature in the Wavenumber–Frequency Domain

MATTHEW WHEELER

NOAA Aeronomy Laboratory, and Program in Atmospheric and Oceanic Sciences, University of Colorado, Boulder, Colorado

GEORGE N. KILADIS

NOAA Aeronomy Laboratory, Boulder, Colorado

(Manuscript received 22 July 1997, in final form 3 April 1998)

ABSTRACT

A wavenumber-frequency spectrum analysis is performed for all longitudes in the domain 15°S–15°N using a long (~18 years) twice-daily record of satellite-observed outgoing longwave radiation (OLR), a good proxy for deep tropical convection. The broad nature of the spectrum is red in both zonal wavenumber and frequency. By removing an estimated background spectrum, numerous statistically significant spectral peaks are isolated. Some of the peaks correspond quite well to the dispersion relations of the equatorially trapped wave modes of shallow water theory with implied equivalent depths in the range of 12–50 m. Cross-spectrum analysis with the satellite-based microwave sounding unit deep-layer temperature data shows that these spectral peaks in the OLR are ''coupled'' with this dynamical field. The equivalent depths of the convectively coupled waves are shallower than those typical of equatorial waves uncoupled with convection. Such a small equivalent depth is thought to be a result of the interaction between convection and the dynamics. The convectively coupled equatorial waves identified correspond to the Kelvin, $n = 1$ equatorial Rossby, mixed Rossby-gravity, $n = 0$ eastward inertio-gravity, $n = 1$ westward inertio-gravity (WIG), and $n = 2$ WIG waves. Additionally, the Madden–Julian oscillation and tropical depression-type disturbances are present in the OLR spectra. These latter two features are unlike the convectively coupled equatorial waves due to their location away from the equatorial wave dispersion curves in the wavenumber-frequency domain.

Extraction of the different convectively coupled disturbances in the time–longitude domain is performed by filtering the OLR dataset for very specific zonal wavenumbers and frequencies. The geographical distribution of the variance of these filtered data gives further evidence that some of the spectral peaks correspond to particular equatorial wave modes. The results have implications for the cumulus parameterization problem, for the excitation of equatorial waves in the lower stratosphere, and for extended-range forecasting in the Tropics.

1. Introduction

a. Motivation

It has long been known that a large part of the synoptic variability in the Tropics is due to propagating disturbances moving parallel to the equator. Such disturbances organize individual convective elements on a spatial scale that is larger than the size of the elements themselves. Well-known examples are the westward propagating synoptic-scale disturbances within the intertropical convergence zones of the tropical ocean basins that were clearly visible in time-longitude plots of cloudiness viewed from early satellites (e.g., Chang 1970). Other examples are now numerous, and such disturbances are of interest not only for their connections to the day-to-day weather of the Tropics, but also from a theoretical standpoint.

About the same time that the first views of tropical cloudiness were received from satellites, a fundamental advance in the understanding of tropical motions was made, namely, the development of the theory of equatorially trapped waves (Matsuno 1966; Lindzen 1967). This theory has since been used to interpret some of the observed propagating disturbances of organized deep convection. Also in the 1960s, the first conclusive observations of equatorially trapped waves in balloon-measured winds of the equatorial lower stratosphere were made (Yanai and Maruyama 1966; Wallace and Kousky 1968). These stratospheric waves, which propagate vertically into the middle atmosphere, have since been proposed to play a role in forcing the quasi-biennial oscillation (QBO; Lindzen and Holton 1968). The links between the observed propagating systems of organized tropical convection, the theory of equatorially trapped

Corresponding author address: Dr. Matthew Wheeler, NCAR/ASP, P.O. Box 3000, Boulder, CO 80307-3000.
E-mail: mwheeler@ucar.edu

waves, and the observed equatorial waves of the lower stratosphere have been the subject of much research and are still not fully understood (e.g., Holton 1972; Lindzen 1974; Chang 1976; Salby and Garcia 1987; Garcia and Salby 1987; Hayashi and Golder 1994; Bergman and Salby 1994; Hayashi and Golder 1997). For this reason there continues to be considerable interest in the way tropical convection is organized in terms of its dominant frequencies and wavenumbers.

The subject of this paper concerns the identification of preferred time- and space scales of synoptic to planetary zonally propagating waves in deep tropical convection. The approach utilizes a wavenumber-frequency spectral analysis of satellite-observed outgoing longwave radiation (OLR), a proxy for cloudiness, and a wavenumber-frequency cross-spectrum analysis with satellite-derived deep-layer tropospheric temperatures. Such methods are particularly useful for the separation of phenomena in the time-longitude domain into westward and eastward moving components. This analysis is also conducive to dynamical interpretation in terms of the dispersion relations of particular wave modes. It is found that several statistically significant spectral peaks in the wavenumber-frequency spectra are present, some of which follow the dispersion curves of the equatorially trapped waves. We call the disturbances contributing to these features ''convectively coupled equatorial waves,'' relying on the assumption that OLR is a reasonably good representation of deep tropical cloudiness.

Previous studies have shown that the broad nature of the spectra of tropical clouds is ''red'' in both zonal wavenumber and frequency, but superimposed upon that are some definite spectral peaks, some of which appear to correspond to equatorial wave modes (e.g., Gruber 1974; Zangvil 1975; Takayabu 1994a). Here we are able to extend the results of this earlier work by using a much longer record (approximately 18 years) and a higher temporal resolution (twice daily) dataset. We also use a dataset that is available at all longitudes, thus providing resolution at all planetary zonal wavenumbers, estimate a red background spectrum against which the statistical significance of the OLR signals can be assessed, and utilize cross-spectra between OLR and temperature to demonstrate dynamical coupling.

The make-up of this paper is as follows. Section 1b briefly reviews the theory of equatorial waves. Section 2 describes the data and methodology. Section 3 presents the wavenumber-frequency spectra of the OLR and describes our construction of a red background spectrum for calculations of the significance of the different wave disturbances. In that section we also show the cross-spectra. Section 4 describes the results of performing a wavenumber-frequency filter to the OLR data, from which the geographical distribution of the variance and time-longitude realizations of the convectively coupled disturbances are presented. Section 5 provides a summary of the observational results and puts the disturbances highlighted in this study into context with those of previous studies. Finally, we end with a discussion in section 6, and conclusions in section 7.

b. Equatorial waves

Since we attempt to associate the observed disturbances in the clouds with types of equatorially trapped wave modes, it is worthwhile to briefly review the theory of equatorial waves. Formally, equatorial wave theory begins with a separation of the primitive equations, linearized about a basic state with no vertical shear, governing small motions in a three-dimensional stratified atmosphere on an equatorial β-plane, into the ''vertical structure'' equation and ''shallow water'' equations (e.g., Matsuno 1966; Lindzen 1967). The equatorial wave modes are the zonally (and vertically) propagating, equatorially trapped solutions of the shallow water equations, which are characterized by four parameters: meridional mode number n, frequency ν, planetary zonal wavenumber s, and ''equivalent depth'' h of the ''shallow'' layer of fluid. The equivalent depth is related to the internal gravity wave speed as $c = \sqrt{gh}$, and appears as a separation constant linking the vertical structure equation and the shallow water equations. Here h is also related to the vertical wavelength of free (dry[1]) waves, as will be discussed in section 6, and to the meridional scaling through the relation for the equatorial Rossby radius, $R_e = (\sqrt{gh}/\beta)^{1/2}$, where β is the latitudinal gradient of the Coriolis parameter.

Given the meridional mode number and wave type, the theoretical dispersion relation will fully characterize the wave provided two out of ν, s, and h are specified. It is presumed that tropical waves that are forced by, and those that control, the convective heating are internal modes with wavelike vertical structures. The resulting solutions of the shallow water equations are either symmetric or antisymmetric about the equator. For the divergence or temperature field, which is presumably related to the convection, modes of odd meridional mode number n (as in Matsuno 1966) are symmetric, whereas those of even n are antisymmetric. Of course, the equivalent depth h that best matches the linear equatorial wave theory to the cloudiness signals is an important issue. We explore this issue in this study, and present a more detailed discussion of the significance of the equivalent depth in section 6. First we turn to

[1] We use the terminology ''free'' and ''dry'' interchangeably to refer to internal waves that are freely propagating through the atmosphere without the continual release of latent heat through cloud formation and precipitation. Although such internal modes must initially be ''forced'' by some mechanism such as the release of latent heat in deep convection, their subsequent propagation is governed by dry dynamics only. Such terminology is consistent with Gill (1982) and Chang and Lim (1988), but somewhat different to that in Lindzen (1967) or Holton (1970).

the observations of the convectively coupled waves, which must, by definition, be observable in the clouds.

2. Data and methodology

The primary data used in this study consists of nearly 18 years of twice-daily estimates of outgoing longwave radiation from the National Oceanic and Atmospheric Administration (NOAA) polar-orbiting satellites (Gruber and Krueger 1984) extending from January 1979 to August 1996. Such data have often been used to distinguish areas of deep tropical convection and as a proxy for precipitation (e.g., Arkin and Ardanuy 1989). The two grids per day are a mapping of the daytime and nighttime passes of the satellite to the synoptic times of 0600 and 1800 Z. Such a mapping is accurate to within 6 h and is done in such a way that each synoptic grid contains half daytime and half nighttime data. Before the mapping to synoptic times, the daytime and nighttime passes were independently interpolated in space and time to remove any missing values (Liebmann and Smith 1996). The data from each scanning swath of the satellite are archived on a 2.5° grid allowing representation of high wavenumber features. However, as the sampling occurs in 14 swaths around the globe each day, care must be taken in the interpretation of spectral features around wavenumber 14, as well as wavenumber-frequency features with phase speeds near and greater than the speed of the zonal passage of the sun-synchronous orbits (464 m s^{-1}). We are only interested in slower-moving disturbances in this study.

Additional datasets used to further substantiate the results are gridded daily for both averaged values of deep-layer tropospheric temperatures and geopotential heights at the 1000-hPa level for the 1979–93 period. The deep-layer tropospheric temperatures are derived from radiances measured by the microwave sounding unit (MSU) that has been carried on the same series of NOAA polar-orbiting satellites from which the OLR measurements were made (Spencer et al. 1990). We make use of both the MSU-derived lower-tropospheric (surface–300 hPa) temperature and upper-tropospheric (500–100 hPa) temperature. The lower-tropospheric temperature is based on a linear combination of MSU channels 2 and 3 (hereafter denoted as MSU23) and the upper-tropospheric temperature is based on a linear combination of channels 3 and 4 (hereafter denoted as MSU34). The averaging kernel for MSU23 peaks near 500 hPa and has most of its radiant energy originating below 300 hPa. The surface contribution over the oceans is very small. For MSU34 the peak in the averaging kernel is near 250 hPa, and most of its signal is received from the 500–100-hPa layer. The MSU is essentially insensitive to nonprecipitating clouds, either cirrus or liquid phase clouds, although the radiances can be contaminated by precipitation-size ice particles in deep convection. Fortunately, the intense ice precipitation events that affect the measured radiances are relatively infrequent and are mostly screened out due to their isolated nature and the scanning of the instrument (Spencer et al. 1990). Thus the MSU provides a good means of observing daily tropospheric temperature variations, even in the presence of clouds and tropical convection. Finally, daily averaged 1000-hPa geopotential heights of the National Centers for Environmental Prediction (NCEP)/National Center for Atmospheric Research (NCAR) 40-Year Reanalysis Project are also used (Kalnay et al. 1996). Both the MSU and 1000-hPa geopotential height data are on the same 2.5° lat × 2.5° long grid as the OLR.

The method used for the first part of this study is space–time spectral analysis. This technique is particularly useful for the study of zonally propagating waves as it decomposes a field of data dependent on time and longitude into wavenumber and frequency components for eastward and westward propagating waves, as well as zonal-mean fluctuations (Hayashi 1982). Since we are interested in synoptic to intraseasonal timescales, our main results (those of the OLR power) are based on spectral quantities that have been calculated for many successive overlapping (by 2 months) 96-day segments of the multiyear OLR dataset. The results are not sensitive to this overlap. To help prevent aliasing, the first three harmonics of the seasonal cycle are removed. Then for each segment the mean and linear trend are removed in time by a least squares fit, and the ends of the series are tapered to zero. The data windowing provided by the tapering helps to minimize the effects of spectral leakage, and the overlapping of segments minimizes the loss of data by the tapering. After tapering, complex FFTs are performed in longitude to obtain Fourier coefficients (in zonal planetary wavenumber space) for each time and for each latitude. Further complex FFTs are applied in time to these coefficients to obtain the wavenumber-frequency spectrum for each latitude. Finally, the OLR power is averaged over all available segments of the 18-yr record, and is further summed for the latitudes between 15°S and 15°N. The resulting effective bandwidth is 1/96 cycles per day (cpd) in frequency, and 1 unit zonal wavenumber. The total number of degrees of freedom (dof), treating each latitude and each (nonoverlapping only) 96-day segment of the 17.67-yr OLR record as an independent realization, is about 1750 ($\approx 2 \times 13 \times 17.67 \times 365/96$). As each latitude cannot be considered to be independent, however, a more conservative estimate would be about 1000 dof. The dof are reduced accordingly when calculations of power are made using the symmetric or antisymmetric components of OLR (as defined below) only, and also when the calculations of power do not use the full 18-yr record.

Cross-spectra are also obtained. They are done in a similar way to the OLR power calculations just described, except that in this case we use successive overlapping 128-day segments of the deseasonalized multiyear datasets, and the data are daily averaged. Aver-

aging of the co- and quadrature-spectral quantities for the many segments of the 15-yr record, and for the latitudes between 15°S and 15°N, is performed prior to creating the coherence-squared and phase. The effective bandwidth is 1/128 cpd in frequency and 1 unit wavenumber. A conservative estimate of the number of dof of these coherence calculations is about 600, and these dof are split equally between the antisymmetric and symmetric components (as defined below).

As mentioned, the method also makes use of an antisymmetric–symmetric decomposition whereby the gridded fields (e.g., OLR) that are a function of latitude, ϕ, can be written as $\mathrm{OLR}(\phi) = \mathrm{OLRA}(\phi) + \mathrm{OLRS}(\phi)$, where $\mathrm{OLRA}(\phi) = [\mathrm{OLR}(\phi) - \mathrm{OLR}(-\phi)]/2$ is the antisymmetric component, and $\mathrm{OLRS}(\phi) = [\mathrm{OLR}(\phi) + \mathrm{OLR}(-\phi)]/2$ is the symmetric component. As discussed in the previous section, linear equatorial waves are either symmetric or antisymmetric about the equator depending on the parameter considered. It is also the case that, in such a linear decomposition, when the power in the antisymmetric and symmetric components are summed, and also summed over the same latitudes in both hemispheres, then this power is identical to the power of the total field summed for the same latitudes. By studying the latitudinally summed power of the antisymmetric and symmetric components we are thus accounting for all the variance of the total field for these latitudes. Additionally, for the cross-power of antisymmetric and symmetric components, the interpretation must be in terms of the amount of the power explained in one component only, not of the power of the total field.

The OLR power spectral results that we present in section 3 extend up to a planetary wavenumber 15 and from a frequency of 1/96 cpd to 0.8 cpd, a range for which we estimate that this dataset has useful information. Due to the red nature of the calculated power spectra, we are little concerned with the folding of high wavenumber and frequency power about the Nyquist limits. Only three obviously erroneous peaks in the power spectra could be detected within the range we studied. These were at eastward wavenumber 14 and periods of 9 and 4.5 days, and also at westward wavenumber 14 and a period around 1.27 days. These spurious peaks can be explained by the aforementioned 14 swaths recorded per day, the slow precession of the orbit that takes about 9 days, and the folding of various harmonics about the frequency of 0.5 cpd. For presentation purposes, the OLR power estimates at these points in the wavenumber-frequency domain were flagged as special values and not plotted. The same flagging of special values was applied to the cross-spectral results from the MSU data as it too suffers from sampling biases of the polar-orbiting satellites.

Another noteworthy characteristic of wavenumber-frequency spectra is that standing waves are represented as equal amounts of variance, at a particular wavenumber and frequency, in both the westward and eastward components. In this study, it is found that no statistically significant disturbances appear as both eastward and westward at the same wavenumber and frequency, so there is no complication of standing waves contributing to the spectral peaks.

Finally, the wavenumber-frequency filtering of the OLR data, as presented in section 4, is performed by taking the inverse of the space–time transform process including only those Fourier coefficients that are within the specified region of interest of the wavenumber-frequency domain. Compared to the forward process described above, however, we accomplish the inverse process by first performing the forward process on the full 18-yr record rather than breaking up the time series into individual 96-day segments. In this way we can retrieve the filtered time-longitude data for the full record. Note that we are again careful to taper the ends of the 18-yr series to zero and remove the first three harmonics of the seasonal cycle before this procedure. Also, since the number of frequency bins increases with an increase in the length of the series, the minimum number of coefficients included in any of the specified regions of the wavenumber-frequency domain used for filtering is 735. This large number of coefficients included in the inverse transform process helps to prevent ''ringing'' of the filtered data, as can be seen in the time-longitude plots of the filtered data in section 4.

3. Wavenumber-frequency spectra

a. Raw OLR power spectra

Figures 1a and b show contours of the logarithm of the power in the antisymmetric and symmetric components of OLR, respectively. The most striking feature of these spectra is their very red nature in both wavenumber and frequency, although notable differences between eastward and westward as well as symmetric and antisymmetric components can be discerned. The feature with the most power in either component or in either propagating direction is the Madden–Julian oscillation (MJO; Madden and Julian 1994), occurring mostly at eastward wavenumbers 1, 2, and 3, and centered at a period of about 48 days in OLRS, and to a lesser extent in OLRA. At frequencies less than about 0.1 cpd, there is greater variance in OLRS than OLRA for almost all wavenumbers except at wavenumber 0, where it is about equal. At higher frequencies around 0.2 to 0.3 cpd and also near wavenumber 0 the power in OLRA becomes much more dominant. At even higher frequencies from around 0.4 to 0.8 cpd it is quite evident that there is more power in westward versus eastward moving waves in both OLRA and OLRS.

Besides these general features, any detailed features of the raw power spectra are somewhat obscured by the redness of the spectrum. The search for any equatorial wave modes is dependent on the identification of ''ridges'' in the contours. For this reason we define a

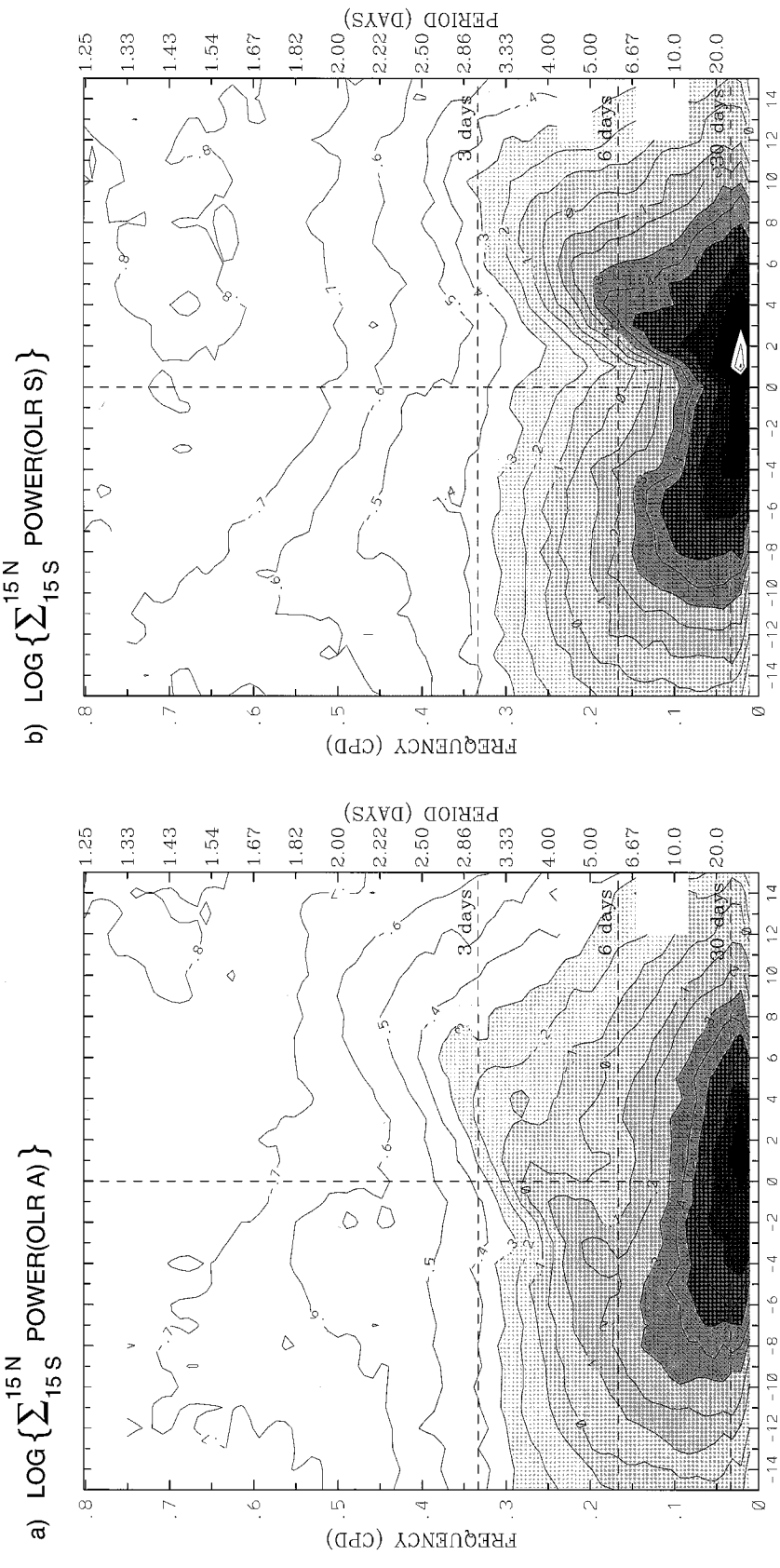

FIG. 1. Zonal wavenumber-frequency power spectra of the (a) antisymmetric component and (b) symmetric component of OLR, calculated for the entire period of record from 1979 to 1996. For both components, the power has been summed over 15°S–15°N lat, and the base-10 logarithm taken for plotting. Contour interval is 0.1 arbitrary units (see text). Shading is incremented in steps of 0.2. Certain erroneous spectral peaks from artifacts of the satellite sampling (see text) are not plotted.

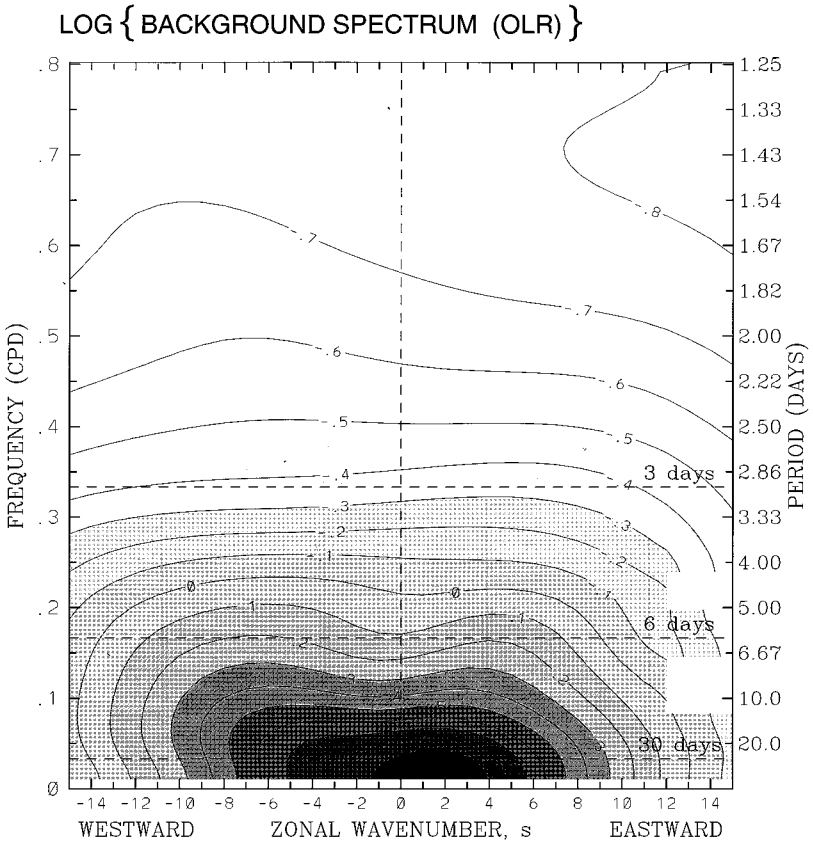

FIG. 2. Zonal wavenumber-frequency spectrum of the base-10 logarithm of the ''background'' power calculated by averaging the individual power spectra of Figs. 1a and 1b, and smoothing many times with a 1-2-1 filter in both wavenumber and frequency. The contour interval and shading are the same as in Fig. 1.

red background spectrum, which we then remove from the original spectra, leaving the statistically significant spectral peaks. The determination of this background is the subject of the next subsection.

b. Background OLR spectrum

The background spectrum used is presented in Fig. 2. It is calculated by averaging the power of OLRA and OLRS, and smoothing many times with a 1-2-1 filter in frequency and wavenumber. The number of passes of the 1-2-1 filter we have used is 10 in frequency throughout, and from 10 to 40 in wavenumber, being 10 at low frequencies and 40 at higher frequencies increasing in two different steps. This smoothing is applied in an attempt to remove any periodic signals that may be present in the spectra at a particular wavenumber and frequency, so that the background may characterize random or nonperiodic processes only. As the smoothing is conservative, the total power of the background, summed over all wavenumbers and frequencies, is still identical to that of an average of the total power of the antisymmetric and symmetric components. However, the background power is not necessarily identical for eastward and westward components, presumably because there are basic-state winds that are advecting clouds systematically in one direction, or because the smoothing has not removed all of the systematic wave propagation. Finally, the background power, by definition, is the same for antisymmetric and symmetric components.

Inspection of Fig. 2 reveals that this defined background is quite smooth, and basically red, with greatest power at the lowest frequencies and wavenumbers. Nevertheless, it does contain some of the general shape characteristics of the individual spectra of Figs. 1a and 1b. It is thus likely that the background still retains some features influencing its shape that might be absent without any periodic wave signals. However, it still has much utility for our understanding, which will become apparent when it is removed from the individual power spectra of Figs. 1a and 1b.

c. Statistically significant spectral peaks in OLR

Dividing the individual power spectra of Figs. 1a and 1b by the background power of Fig. 2 yields the contour plots shown in Figs. 3a and 3b. The resulting contours

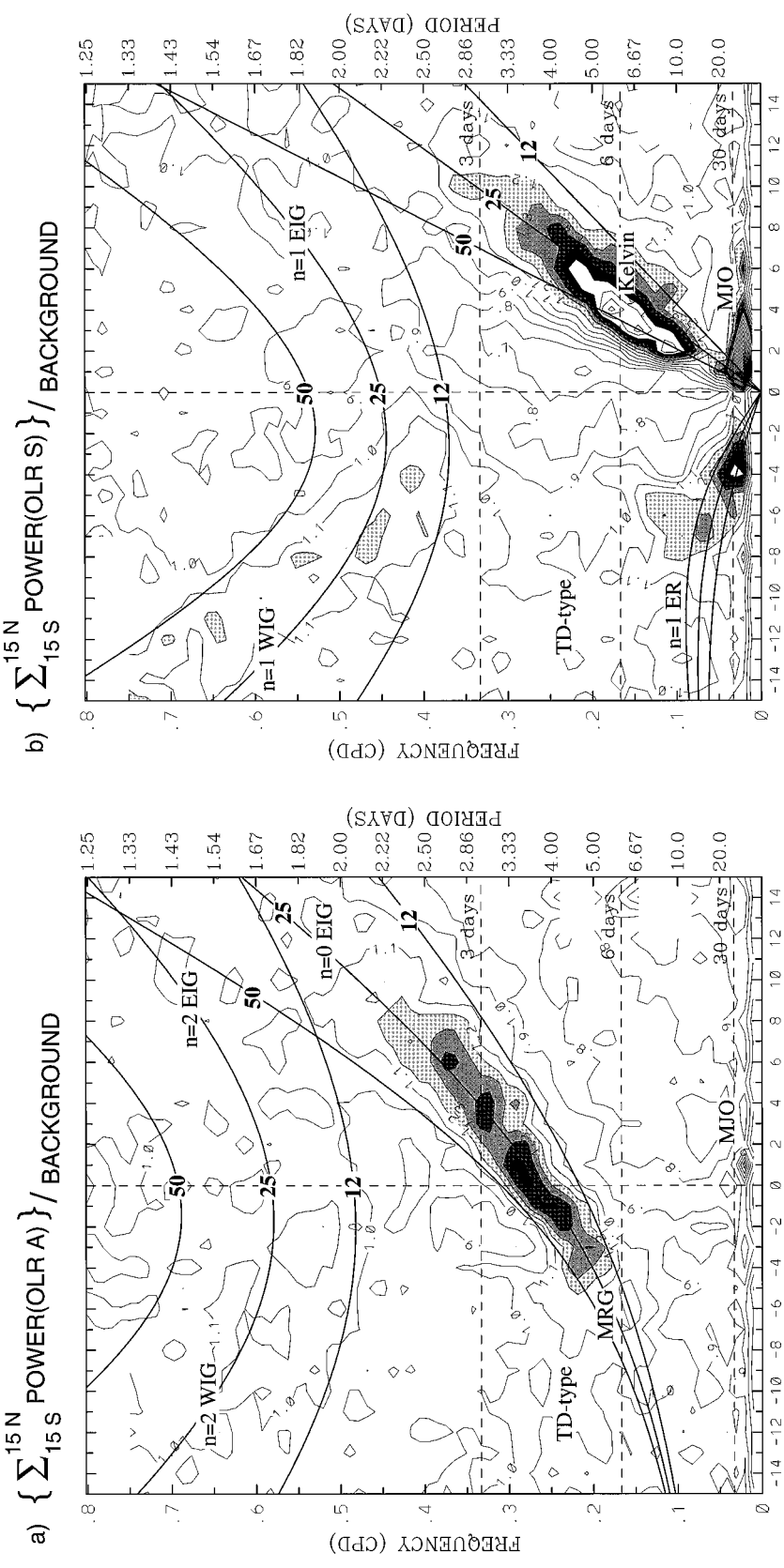

FIG. 3. (a) The antisymmetric OLR power of Fig. 1a divided by the background power of Fig. 2. Contour interval is 0.1, and shading begins at a value of 1.1 for which the spectral signatures are statistically significantly above the background at the 95% level (based on 500 dof). Superimposed are the dispersion curves of the even meridional mode-numbered equatorial waves for the three equivalent depths of $h = 12$, 25, and 50 m. (b) Same as in panel a except for the symmetric component of OLR of Fig. 1b and the corresponding odd meridional mode-numbered equatorial waves. Frequency spectral bandwidth is 1/96 cpd.

can be thought of as levels of significance, with peaks in the individual spectra that are significantly above (at the 95% level for 500 dof) the background shown as shaded. Superimposed upon these two plots are the dispersion curves for even and odd meridional mode number equatorial waves, for various equivalent depths and for a zero wind basic state. The correspondence between the dispersion curves and regions of the wavenumber-frequency domain significantly above the background is good.

Concentrating on the areas of significance corresponding to the dispersion curves, we see signals of ($n = -1$) Kelvin, $n = 1$ equatorial Rossby (ER), $n = 0$ mixed Rossby-gravity (MRG), $n = 0$ eastward inertio-gravity (EIG), $n = 1$ westward inertio-gravity (WIG), and $n = 2$ WIG waves. The eastward moving counterparts of the $n = 1$ and $n = 2$ inertio-gravity waves cannot be discerned, nor can higher meridional mode ER waves. The dispersion curves that best match the wavenumber-frequency characteristics of these waves have equivalent depths in the range of about $h = 12$–50 m, which is about an order of magnitude smaller than that for a free wave generated as the peak projection response to deep convective heating, as will be discussed in section 6. Based on this forthcoming discussion, such shallow equivalent depths are likely the result of the way convection is interacting with the dynamics. The association between the spectral signals in the convection and the dynamics will be examined in the next subsection.

Further inspection of the figures shows the statistically significant appearance of the MJO in OLRS at a constant frequency around 0.025 cpd for the range of eastward planetary wavenumbers of 1 through to about 7, which is not along any of the theoretical equatorially trapped wave dispersion curves. The extension of the signal of the MJO to wavenumbers that are higher than what is considered usual for this planetary-scale phenomenon is due to the localization of the power of the convectively coupled part of this disturbance to the Eastern Hemisphere (Salby and Hendon 1994). Inspection of a similar plot, but calculated using a narrower frequency bandwidth (not shown), reveals the separation of the MJO from the Kelvin wave signal even at wavenumber 1, with a spectral gap in the power ratio occurring at a period of about 25 days.

Another region of the wavenumber-frequency domain where there are areas of significance that do not correspond to the dispersion curves is in the region of westward moving synoptic-scale waves with periods around 3–6 days, mostly in OLRA. Such waves in tropical convection are well documented in previous studies (e.g., Takayabu and Nitta 1993; Dunkerton and Baldwin 1995) and are generally termed ''tropical depression'' (TD) disturbances occurring over a wide range of frequency and wavenumber. There is also a region of significantly large variance around westward moving wavenumber 6 and a period of about 7 days in OLRS. We speculate that this feature is a Doppler-shifted signal of the $n = 1$ ER wave, but we will leave the identification of this peak to further studies. For now, we are most interested in the spectral signals that match the plotted dispersion curves of the equatorial waves.

Further inspection of the signatures of the equatorial waves in the OLR spectra reveals that, in general, the greatest significance is seen for the lower (propagating) wavenumbers, with the significance falling off at around wavenumbers 8–12. For the zonal-mean component, only the $n = 0$ IG wave is significant at a period of about 4 days. The statistical significance also appears to be consistently greater for the lower-frequency phenomena, being greatest for the Kelvin wave, ER wave, and MJO, and least for the $n = 2$ WIG wave. For the Kelvin wave, it is also apparent that the lower wavenumber components propagate faster than the higher wavenumber components. This could be due to the different wavenumber components occurring at different times when the basic zonal flow differs. We leave more detailed discussion of these general features for section 5.

Finally, we note that although the statistical significance of the spectral peaks in Fig. 3 is spread over many wavenumbers and frequencies, most of the power is contained within the peaks at low wavenumbers and frequencies due to the red background. In fact, the amount of power present above the background may be determined by making a subtraction of the background from each of the power spectra of Fig. 1. When this is done (not shown), the most power in the antisymmetric component appears for the MRG wave for wavenumbers of around 2–4. For the symmetric component the most power appears for the MJO, the low wavenumber (and frequency) components of the $n = 1$ ER wave, and the $s = 1$ and 2 Kelvin waves. Such time- and space scales should be reflected in the accompanying atmospheric circulations. As we shall see in section 5, this indeed appears to be the case, especially for the circulations of the lower stratosphere.

d. Cross-spectrum analysis with MSU temperatures

The previous subsection has shown that in OLR there are significant spectral peaks in the wavenumber-frequency domain lying along the dispersion curves of equatorial wave modes. These spectral peaks occur for equivalent depths in the range of 12–50 m. It is of interest to know whether similar spectral peaks occur in dynamical fields, and whether there is an association, or apparent coupling, between the convection and the dynamics for similar equivalent depths. Here we will use the MSU temperatures and 1000-hPa geopotential heights as characteristic dynamical fields for the troposphere. To test these ideas we present wavenumber-frequency cross-spectra between the MSU34 and MSU23 deep-layer temperatures (Figs. 4a,b), between OLR and the MSU23 temperatures (Figs. 4c,d), and between the 1000-hPa geopotential heights and MSU34

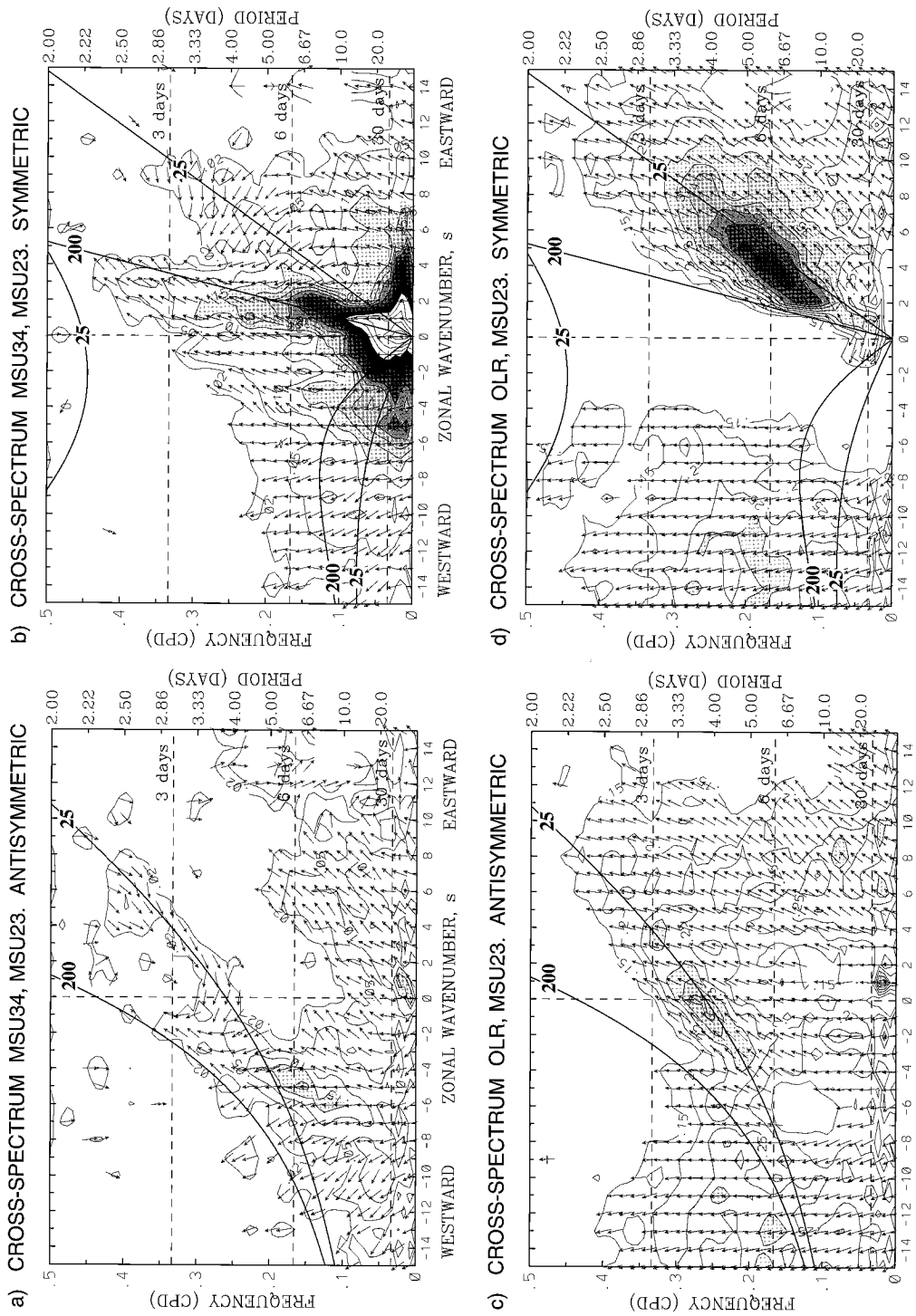

FIG. 4. Coherence squared (contours) and phase (vectors) of cross-spectra between (a) antisymmetric MSU34 and antisymmetric MSU23, (b) symmetric MSU34 and symmetric MSU23, (c) antisymmetric OLR and antisymmetric MSU23, (d) symmetric OLR and symmetric MSU23, (e) antisymmetric 1000-hPa geopotential height and antisymmetric MSU34, and (f) symmetric 1000-hPa geopotential height and symmetric MSU34. The cross-spectra are calculated for the 1979–93 period, and are summed for the latitudes between 15°S and 15°N. The contour interval for coherence-squared is 0.05. In (a), (b), (e), and (f) an additional contour is drawn at 0.02, whereas in (c) and (d) the contouring starts at the level of 0.15. Phase vectors are drawn only

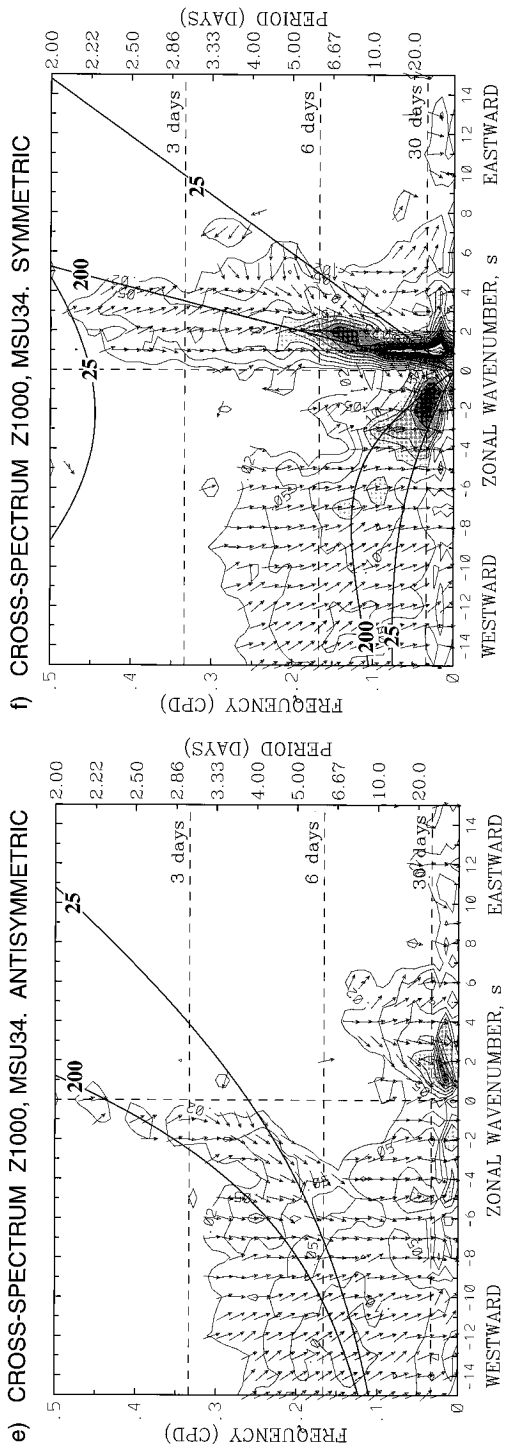

FIG. 4. (*Continued*) for those wavenumbers and frequencies for which the relationship has been determined to be statistically significant at the 95% level (based on 300 dof). Shading starts at the second contour level. Upward-pointing arrows indicate that the fields are in phase. An arrow pointing to the right indicates that the first field is leading the second field by a quarter cycle. Frequency spectral bandwidth is 1/128 cpd. Superimposed are the dispersion curves of the equatorial waves for the two equivalent depths of $h = 25$ and 200 m.

temperatures (Figs. 4e,f). Each calculation has been performed and is presented separately for the antisymmetric and symmetric components of each field. Contours of coherence-squared start at a level that has been determined to show an unbiased statistically significant relationship (at the 95% level for 300 dof; Amos and Koopmans 1963), and phase vectors are drawn only for those points that are significant. Thus these pairs of plots indicate the space and timescales of the dominant variability that is present as either a vertically coherent signal in the dynamics (Figs. 4a,b), as a coherent (coupled) signal between the convection and the dynamics (Figs. 4c,d), or as a coherent signal between two quite different dynamical fields (Figs. 4e,f). Superimposed upon these plots are the dispersion curves for the equatorial waves for the two different equivalent depths of $h = 25$ and 200 m, the former being about the typical scale of the equatorial waves present in the convection as determined in the previous subsection, and the latter being the theoretically determined scale of the peak projection response to an idealized deep tropical convective heating (to be discussed in section 6). It is of interest to see which equivalent depth scale appears most prominently in each plot.

Figure 4b shows the cross-spectrum of the symmetric fluctuations of temperature that are coherent between the lower and upper troposphere. In the region of the Kelvin wave dispersion, both equivalent depth scales are apparent. That is, there appears to be Kelvin waves moving eastward at either about 40 m s^{-1}, or at about 16 m s^{-1}. The former of these is consistent with the Kelvin wave speed found in the same dataset by Bantzer and Wallace (1996), and also in station wind and pressure data by Milliff and Madden (1996). The latter is consistent with the speed of the Kelvin wave identified in the OLR in the previous subsection. The phase vectors indicate that the faster Kelvin wave has a temperature signal that is nearly in phase between the upper and lower troposphere, with the upper-level perturbations slightly leading the lower, while the slower Kelvin wave has the upper-tropospheric temperature lagging the lower-tropospheric temperature by about one-quarter of a cycle. Figure 4a similarly shows the cross-spectrum for the antisymmetric tropospheric temperature fluctuations. Again we see an indication of equatorial wave modes existing for the two separate equivalent depth scales, with a similar robust change in the phase vectors between the two scales.

To test whether the smaller equivalent depth-scale waves in the MSU temperatures of Figs. 4a and 4b are in fact related to the equatorial waves appearing in the OLR (Fig. 3), we examine the cross-spectra between OLR and lower-tropospheric temperature in Figs. 4c and 4d. Note that in these plots we begin the contouring and shading at a slightly higher value of the coherence-squared, as there is a slight bias in this calculation toward in-phase coherence due to the contamination of the MSU temperatures by precipitation-sized ice parti-

cles in deep convection (see section 2). Nevertheless, there are still areas of the wavenumber-frequency domain that have much higher coherence than elsewhere, and for these areas the relationship is not exactly in phase. In particular, the regions of the greatest coherence in these plots correspond to the MRG, $n = 0$ EIG, and Kelvin waves with about a 25-m equivalent depth. These areas of high coherence occur for a similar range of wavenumbers and frequencies as for the variations in OLR alone (Fig. 3). For the MRG and $n = 0$ EIG waves the coherence-squared peaks at a value of 0.40, thus these waves account for around 40% of the tropical variance of antisymmetric MSU23 temperatures at these wavenumbers and frequencies. For the Kelvin wave the coherence-squared peaks at a value of about 0.55. The phase relationship in each of these areas of peak coherence is consistently that of the convection slightly leading (by about one-eighth of a cycle) low MSU23 temperatures. In contrast to the high coherence between the OLR and MSU23 for these aforementioned waves, the $n = 1$ ER wave does not appear. Presumably this wave does not have a strong relationship with the lower-tropospheric temperature, or its coherent relationship is canceled by other variability that has an opposite relationship. Nevertheless, the strong coherence shown by the Kelvin, MRG, and $n = 0$ EIG waves would suggest that all of the equatorial wave modes shown to be present in the OLR spectra (Fig. 3) are ''coupled'' with the dynamics. It turns out that these convectively coupled equatorial waves have wavenumber-frequency characteristics that are quite distinct from those that are most prominent in the dynamics alone.

To further explore the (presumably) nonconvectively coupled equatorial waves that correspond to the $h \sim$ 200-m equivalent depth, we look at the cross-spectrum between the 1000-hPa geopotential heights and the MSU34 temperatures (Figs. 4e,f). These two fields were chosen because Milliff and Madden (1996) and Bantzer and Wallace (1996) have previously identified the fast ($\sim$40 m s^{-1}) Kelvin waves in these or similar parameters. We now see that the regions of largest coherence-squared now lie preferentially along the $h = 200$-m equivalent depth dispersion curves for each of the different wave types present in this wavenumber-frequency domain. In the regions of this high coherence the phase relationship tends to be such that warm MSU34 temperatures are slightly (by less than one-eighth of a cycle) leading low values of 1000-hPa height. The wavenumber-frequency characteristics of these equatorial waves are quite distinct from those of the convectively coupled equatorial waves of Fig. 3.

Hence we have been able to show that the so-called convectively coupled equatorial waves do show a coherent relationship with a dynamical field, and these waves are somewhat distinct from the most prominent equatorial waves that appear in the dynamical fields alone. For the rest of this paper we concentrate on the convectively coupled waves identified in section 3c.

e. Seasonal modulation of the OLR spectra

It is possible that what appears in Fig. 3 is a smeared version of some much more concentrated (in wavenumber and frequency) spectral peaks occurring at different times and in different parts of the wavenumber-frequency domain. Hence, it is of interest to know how robust the spectral peaks of the convectively coupled equatorial waves in the OLR are for independent samples of the 18-yr record. Presumably, the convectively coupled waves would be influenced by the basic state that they develop in. Some important components of the basic state that are known to have an influence on theoretical and modeled convectively coupled waves are the basic-state winds (e.g., Zhang and Webster 1989; Zhang and Geller 1994; Xie and Wang 1996) and the underlying sea surface temperature (SST) (e.g., Hess et al. 1993). These components of the basic state vary with the seasonal cycle and also on interannual timescales with the El Niño–Southern Oscillation (ENSO) phenomenon.

Figure 5 presents the contours of significance, as in Fig. 3, for two opposite phases of the seasonal cycle: southern summer, extending from November to April, and northern summer, extending from May to October. It should be noted that we divide by the same background as in Fig. 2 for the full 18-yr period, allowing us to compare the variability between the seasons more directly. Note that the definition of the seasonal cycle was based on the times of the year when the latitude of maximum mean tropical convection is either south or north of the equator (see Meehl 1987). Some differences in the type of variability acting during these two phases of the seasonal cycle are apparent. One obvious difference between the wavenumber-frequency plots is the increased power that occurs at westward wavenumbers of about 6 to 15 and at periods around 2.5 to 6 days for both OLRA and OLRS during May–October. Such an increase in power at these synoptic scales is related to the increased predominance of TD-type disturbances at that time of year, as was previously noted by Dunkerton and Baldwin (1995). The fact that such disturbances are present on only one side of the equator also explains the appearance of the signal in both OLRA and OLRS, unlike the signals of the convectively coupled equatorial waves. The large region of the wavenumber-frequency domain that the TD-type disturbances occupy also differs from the signal of the convectively coupled equatorial waves, whose spectral peaks are stronger and more tightly confined along the dispersion curves.

Apart from the substantially weaker appearance of the TD-type disturbances during southern summer, these plots show that the convectively coupled equatorial wave disturbances, except possibly the $n = 1$ ER wave, do not vary greatly at different times of the year. The MJO is similarly present in both seasons, although at a somewhat reduced magnitude in northern summer, consistent with previous studies (e.g., Salby and Hendon

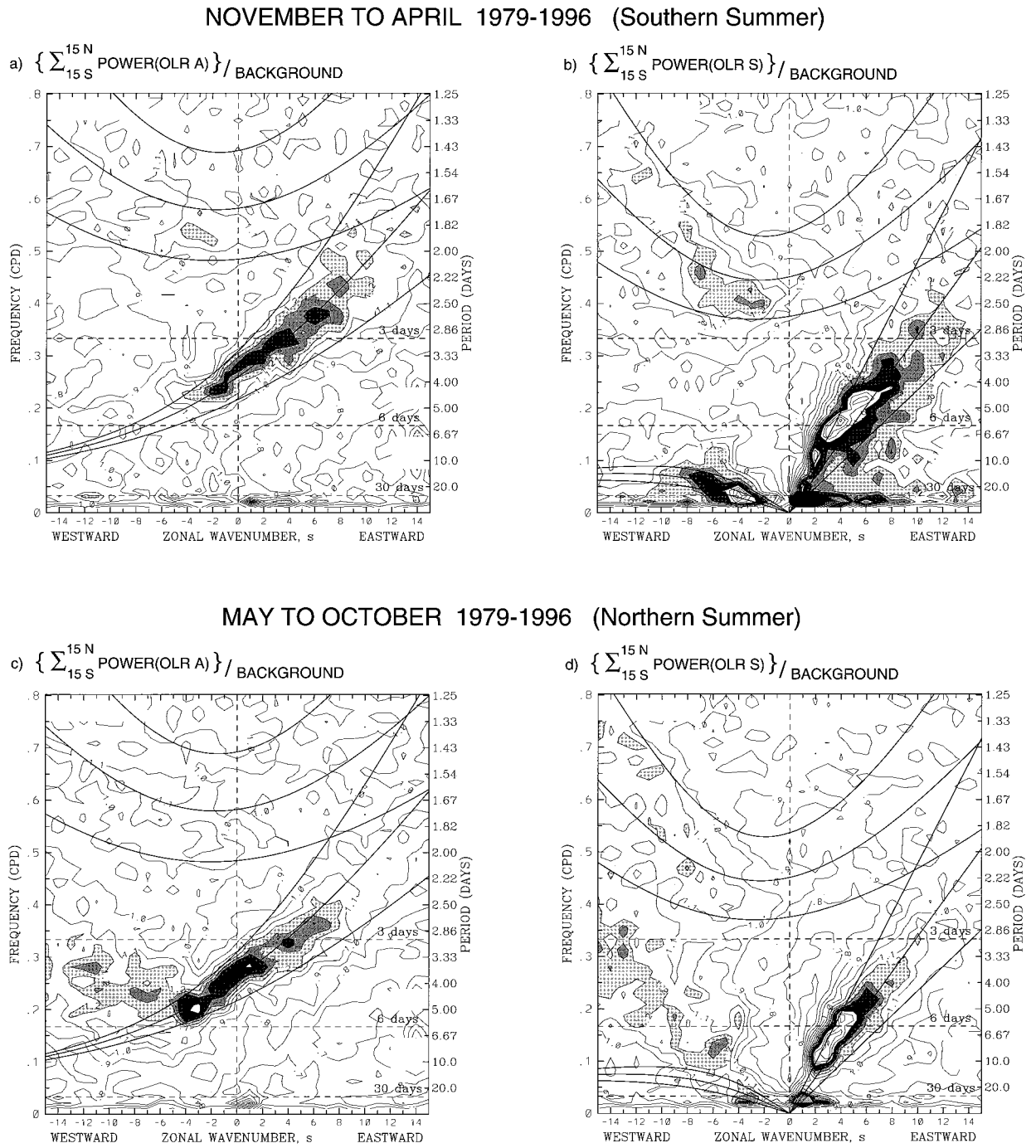

FIG. 5. (a) As in Fig. 3a except for the OLRA power calculated only for the November–April season of the 1979–96 record. Note that the background spectrum used is the same as in Fig. 2. (b) As in panel a except for the OLRS power for the November–April season. (c) As in panel a except for the OLRA power for the May–October season. (d) As in panel a except for the OLRS power for the May–October season.

1994). We thus conclude that the spectral signals of the convectively coupled equatorial waves, as well as the MJO, are quite robust with respect to the seasonal cycle. We also note that the appearance of the spectra is not significantly modified by the phase of ENSO (not shown), although we might expect that the geographical regions where a given wave type occurs may be shifted. This is fortunate, as it means that we can filter the OLR dataset for very specific regions of the wavenumber-frequency domain to retrieve the time-longitude char-

acter of the disturbances that are contributing to the spectral peaks.

4. Wavenumber-frequency filtering

The character of the convectively coupled waves in the time-longitude domain, and for each latitude, can be extracted from the total OLR dataset by filtering in the wavenumber-frequency domain, based on the results of the previous section. Figure 6 displays the defined regions of filtering for each wave and superimposes additional dispersion curves for more widely varying equivalent depths. Each of the convectively coupled equatorial waves we identify is either antisymmetric or symmetric, whereas the MJO is allowed to include both components. The regions of filtering are also drawn such that the outlines are inclusive, meaning that the wavenumber or frequency where the edge of the region is drawn is included in the filtered dataset. So, as an example, for the MJO we include wavenumbers 1–5 and frequencies from 1/96 cpd through to 1/30 cpd. None of the defined regions are overlapping in either the antisymmetric or symmetric components. Note also that we filter for a wider range of equivalent depth (from 8 to 90 m) for the Kelvin, $n = 1$ ER, and MRG waves, than we do for the higher frequency inertio-gravity waves (for which we use from 12 to 50 m). This is simply because of the fact that the lower frequency waves appear to occupy a larger range of equivalent depths, which may be the result of these slower waves being more affected by Doppler-shifting by the basic-state zonal wind. Figure 6a also defines a region for the $s = 0$, $n = 0$ inertio-gravity wave, which is at the zero wavenumber only, and extends over equivalent depths of 8–90 m.

When the filtering of the symmetric, antisymmetric, or total OLR datasets is performed for these regions of the wavenumber-frequency domain, we obtain new OLR datasets that contain the modes of interest, as well as certain elements of the random or nonperiodic events that are contributing to the background spectrum. Without any additional information on the sources of the spectral peaks, this inclusion of the background noise is unavoidable. As shown below, however, the part of the red-noise background that is contained within the filtered data simply appears as a continuum of small amplitude fluctuations, whereas the wave disturbances of interest appear as bursts of high-amplitude activity.

a. Geographical distribution of the OLR variance

Figure 7 presents the geographical distributions of the OLR variance for the seasons of southern summer and northern summer for each of the different wavenumber-frequency bands. For comparison, the first set of maps (Figs. 7a,b) shows the variance for all scales considered here, which goes from wavenumber 0 to 15, and frequencies from 1/96 cpd to 0.8 cpd. This encompasses the entire domain displayed in Fig. 1, and can be considered to contain all planetary to synoptic scales. These two maps display the well-documented shift of the maximum variance of the tropical convection from south of the equator in southern summer to north of the equator in northern summer (see also Lau and Chan 1988). The main centers of convective variance on these scales lie over the Indian to western Pacific Ocean sectors, South America, and Africa. Note that the contour interval for these first two maps is 10 times that of the following ones.

The next two maps (Figs. 7c,d) present the geographical distribution of the OLR variance for the MJO-band for the respective seasons. The MJO, defined here as having both symmetric and antisymmetric components about the equator, also shifts its latitudinal position throughout the year. Consistent with other studies (e.g., Weickmann and Khalsa 1990; Salby and Hendon 1994), the variance of the MJO-band is mostly confined to the eastern Indian Ocean and western Pacific sectors, and in these regions can be seen to explain more than 10% of the variance of all the scales presented in Figs. 7a and 7b.

Moving on to the geographical distributions of the variance of the different equatorial waves, we present in Figs. 7e and 7f the variance of the convectively coupled Kelvin wave. Compared to the convective signal of the MJO, the OLR variance of the convectively coupled Kelvin wave is of a similar magnitude, is more global in its occurrence, and more confined to the equator. It also occurs throughout the year, but with a maximum of variance in southern summer, especially in the Atlantic sector.

Figs. 7g and 7h display the geographical distribution of variance for the convectively coupled $n = 1$ ER wave. Like the Kelvin wave, this wave is symmetric, yet we see that the variance of its OLR signal is maximized off the equator at about 12° lat. This is consistent with the theoretical shallow water ER wave, which has maximum divergence off the equator (Matsuno 1966), and is also consistent with previous observations of such waves (Kiladis and Wheeler 1995). The wave also has a nonzero convective signal on the equator, as in the theoretical structure. Further, the signal of the convectively coupled ER wave is maximized in southern summer throughout the Indian to western Pacific sectors. In the regions of northern Australia or the Philippines, the variance is greater than that of the convectively coupled Kelvin wave, and is comparable to that of the MJO.

Compared to that of the $n = 1$ ER wave, the variance of the convectively coupled MRG wave (Figs. 7i,j) is of a smaller magnitude and is shifted to a position centered on the dateline, to the east of the main center of far western Pacific convection. This location, as well as its maximum variance in our defined northern summer season, is consistent with that found in the observational study of Hendon and Liebmann (1991). It is also notable that the locations of maximum variance, at about 8° lat,

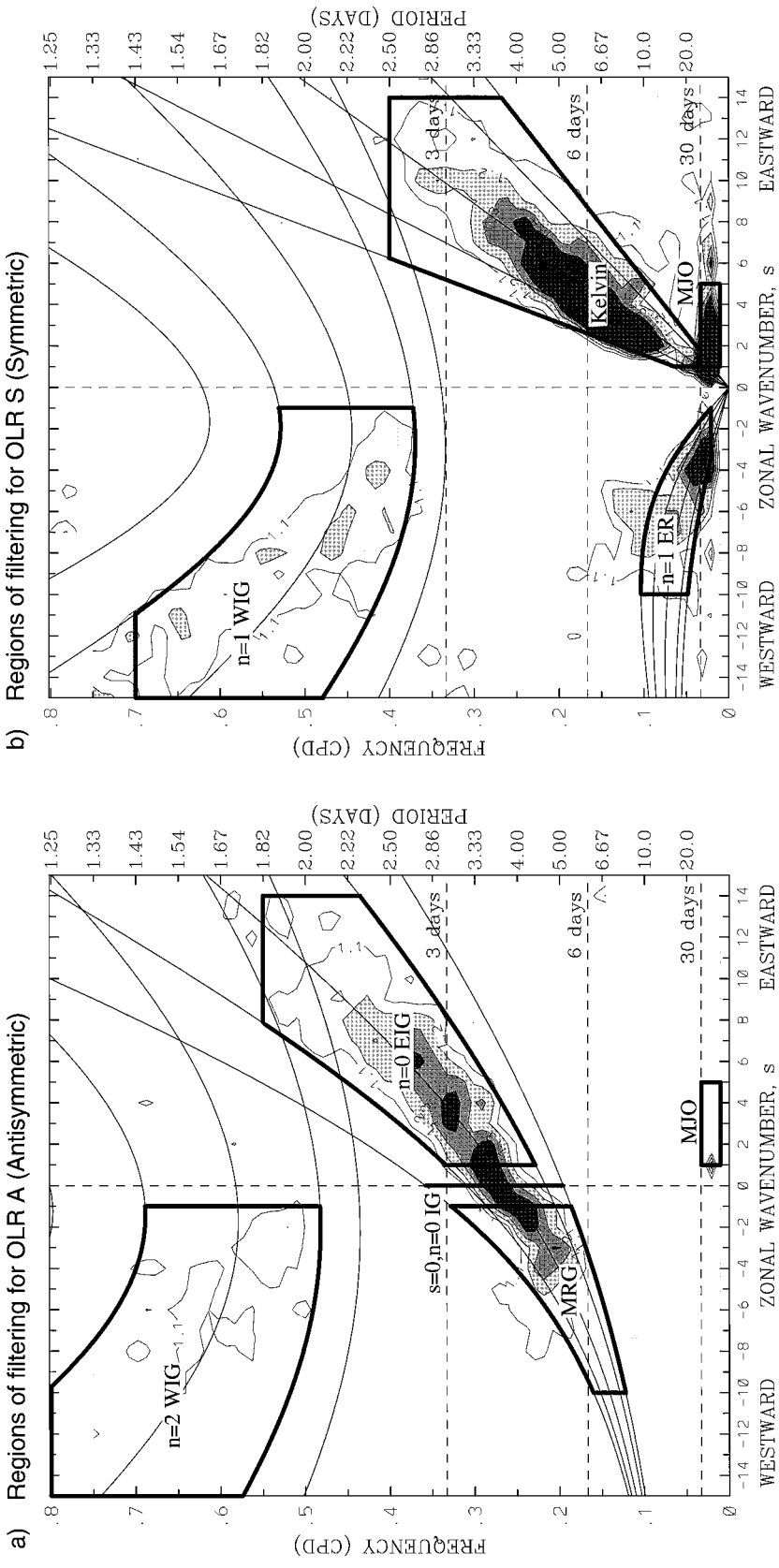

FIG. 6. As in Fig. 3 excluding contours less than 1.1 and greater than 1.4. Thick boxes indicate the regions of the wavenumber-frequency domain used for filtering of the OLR dataset to retrieve the longitude-time information of the convectively coupled tropical waves for the (a) antisymmetric component and (b) symmetric component of the OLR. The thin lines are the various equatorial wave dispersion curves for the five different equivalent depths of $h = 8$, 12, 25, 50, and 90 m.

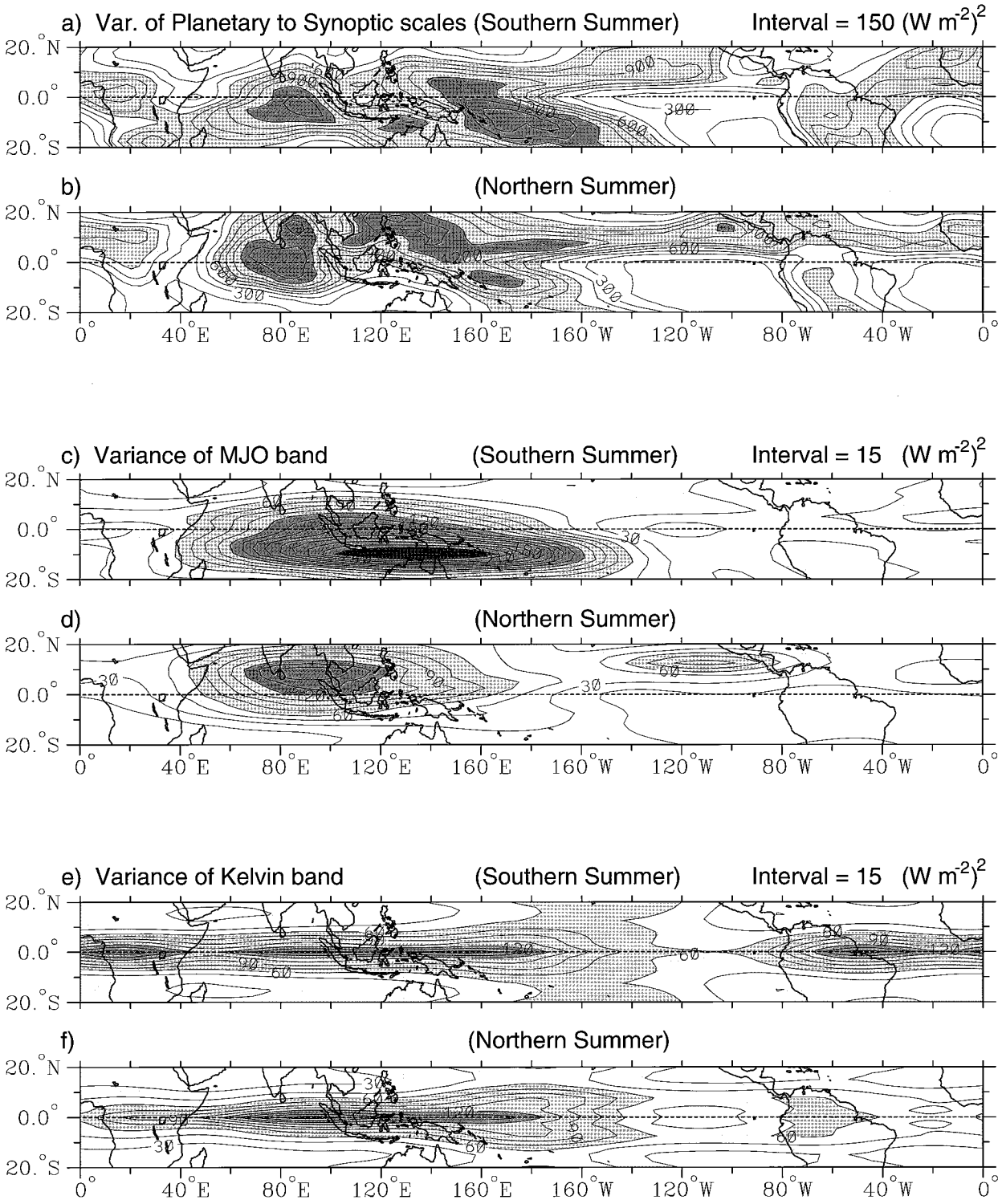

FIG. 7. Geographical distributions of the OLR variance for various parts of the wavenumber-frequency domain of interest. (a) and (b) All planetary to synoptic scales for southern summer and northern summer, respectively. (c) and (d) The MJO-filtered band. (e) and (f) The Kelvin wave–filtered band.

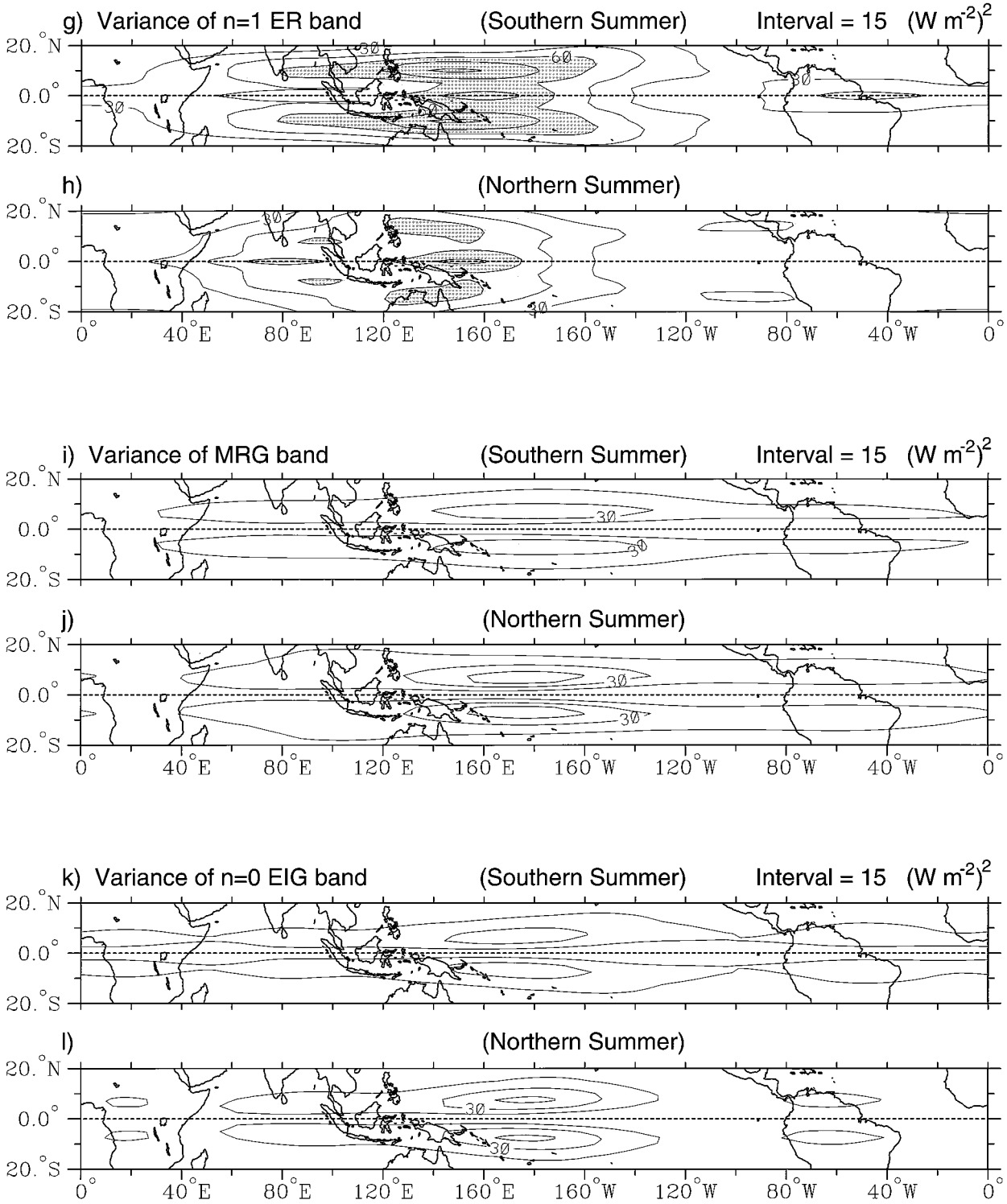

FIG. 7. (*Continued*) (g) and (h) The $n = 1$ ER wave band. (i) and (j) The MRG wave–filtered band. (k) and (l) The $n = 0$ EIG wave–filtered band.

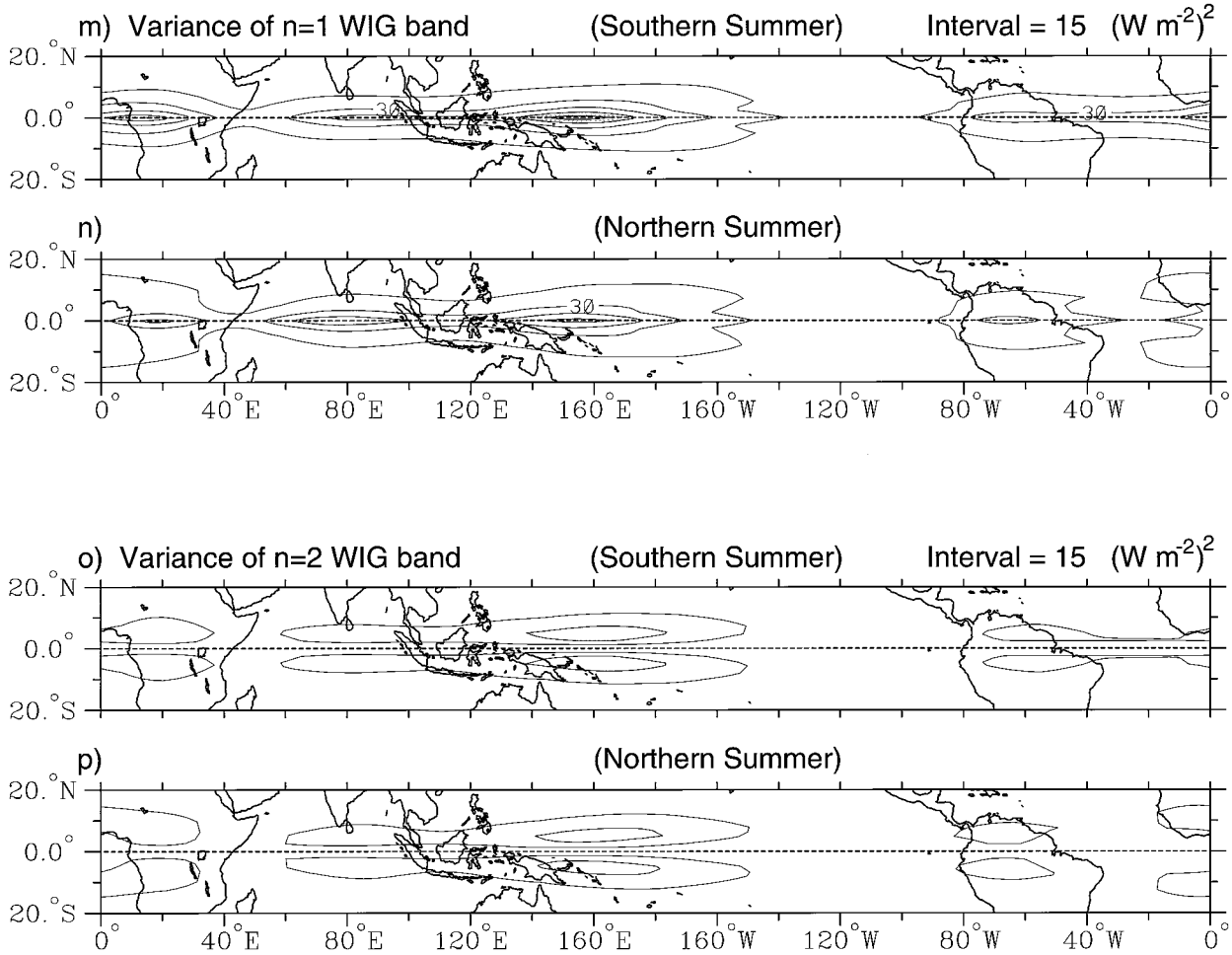

FIG. 7. (*Continued*) (m) and (n) The $n = 1$ WIG wave–filtered band. (o) and (p) The $n = 2$ WIG wave–filtered band. Contour interval is 150 (W m^{-2})^2 in (a) and (b), and 15 (W m^{-2})^2 otherwise. See text for further details.

are shifted equatorward compared to that of the convectively coupled $n = 1$ ER wave. This equatorward shift is also noticeable for the $n = 0$ EIG and $n = 2$ WIG waves (Figs. 7k, 7l, 7o, and 7p). This detail is a further consistency between the shallow water theory and these observed waves (as can be seen, e.g., in Fig. 1 of Takayabu 1994a), and the equivalent depth that can be calculated from this meridional scaling is within the range of those calculated from the spectra. Note, however, that this last calculation involves some uncertainty due to the fourth-root dependence of the meridional scaling to the equivalent depth.

Variance of the convectively coupled $n = 0$ EIG wave (Figs. 7k,l) is of a similar magnitude to the convectively coupled MRG wave, and is also centered at about the dateline and off the equator. The $n = 1$ WIG wave (Figs. 7m,n), on the other hand, is maximized on the equator, and is situated more to the west and within the envelope of the main convection. The OLR variance of this wave is even more confined to the equator than that of the convectively coupled Kelvin wave, yet another consistent feature between these observations and the shallow water equatorial waves. Finally, the geographical distribution of the variance of the $n = 2$ WIG wave band is displayed in Figs. 7o and 7p. It is maximized off the equator, centered around 160°E, and shows little seasonal variation. This convectively coupled wave mode explains the least amount of OLR variance of all of the wave types isolated in this study.

b. Time-longitude realizations

The final results of this paper are a presentation of the wave-type-filtered OLR datasets for a sample 6-month period, and for comparison, the total OLR field for this same period. The 6-month period that we have chosen to display extends from September 1992 to the end of February 1993, which brackets the period of intensive observations of the Tropical Ocean Global Atmosphere (TOGA) Coupled Ocean–Atmosphere Response Experiment (COARE; Webster and Lukas 1992). This is a period of special interest for many researchers

studying large-scale circulation and convection (e.g., Takayabu 1994b; Gutzler et al. 1994; Lin and Johnson 1996; Chen et al. 1996).

We first present the time-longitude section of the total OLR field (Fig. 8), shown at its full 2.5° long and twice-daily time resolution. The OLR has been averaged over 10°S–2.5°N, which brackets the mean latitudinal position of maximum convective activity during this northern fall to southern summer period. The three longitudinal centers of maximum convective activity clearly stand out, as does diurnal variability. Also prominent is the organization of convective activity into zonally propagating systems. We may classify many of these propagating systems as different convectively coupled equatorial wave modes, such as those features indicated by the black lines, circles, and crosses. First we will examine the convective signals that can be associated with the MJO.

Figure 9a shows the same time-longitude section as Fig. 8, but for the MJO-filtered band only. We see that the negative anomalies of the MJO comprise the slow progressions of convective activity from the Indian Ocean to the western Pacific, most prominent in this example during December and January. The two major events of December and January are propagating eastward at about 4 and 6 m s^{-1}, respectively, and appear to be dominated by zonal wavenumber 2, quite typical of the MJO (Madden and Julian 1994). In contrast, the convectively coupled Kelvin wave (Fig. 9b) is much faster, and can be seen to have much more widely varying time and space scales during these 6 months. Many of the individual events displayed in this figure can be readily identified in the total field. Concentrating first on the late December to early January period, we see that there is quite a broad wavenumber 1 component evident, which is highlighted with the long continuous and dashed lines drawn on Figs. 8 and 9 for a phase speed of about 18 m s^{-1}. These dashed lines in fact extend around the globe. This wavenumber 1 convectively coupled Kelvin wave component is evident in the total field as well, starting in the South American and Atlantic sectors and propagating all the way into the Indian and western Pacific Ocean sector. In February there are more strong signatures of the convectively coupled Kelvin wave, one of which is highlighted with a dotted line in the Eastern Hemisphere. This second case can be seen to have a higher wavenumber component and a phase speed of around 16 m s^{-1}.

Turning now to the OLR anomalies of the $n = 1$ ER wave-filtered dataset during this period (Fig. 9c), we see that one of the most prominent features is in the form of a wave packet around the period of mid November to mid December at about 160°E. The large-scale circulations associated with these particular ER waves was discussed by Kiladis and Wheeler (1995). The individual elements of this wave packet are propagating to the west with a phase speed of about 5 m s^{-1} (as marked with lines), while the group speed has a slow eastward component. These marked features are also evident within the total OLR field as a fluctuation with a timescale around 15 days. The amplitude of the anomalies produced by this wave type are quite significant, being greater than 20 W m^{-2} during this case.

The OLR signals of the convectively coupled MRG wave are displayed in time-longitude form in Fig. 9d. In this plot the contour interval is reduced to 6 W m^{-2}, because this wave has a smaller amplitude signal than the other convectively coupled planetary-scale waves, which is partly the result of averaging the antisymmetric OLR signal over latitudes that span the equator. This wave is also noticeably organized into wave packets, like the $n = 1$ ER wave, but unlike the convectively coupled Kelvin wave. The group progression of convectively coupled MRG waves is to the east at around 5 m s^{-1}, whereas the individual phases, as highlighted by three crosses during September, are propagating to the west at fairly widely varying phase speeds of around 20 m s^{-1}. These three highlighted features are also noticeable in the total OLR field.

Turning now to the higher-frequency inertio-gravity waves, we combine the filtered anomalies of the $n = 0$ EIG and $s = 0$, $n = 0$ IG waves in Fig. 9e, and we combine the filtered anomalies of the $n = 1$ WIG and $n = 2$ WIG waves in Fig. 9f. The small circles of Fig. 9e highlight some strong phases of the $n = 0$ EIG waves, and the large circle of Fig. 9f outlines a particularly strong group of WIG waves. These, respectively, 3-day and 2-day timescale waves are also discernible in the total OLR field. Again, we also see noticeable group progressions for these waves, being eastward for the $n = 0$ EIG waves and westward for the WIG waves. Typical phase speeds are around 25–50 m s^{-1} for the $n = 0$ EIG wave and 15–35 m s^{-1} for the WIG waves. Spatial scales are on the order of 1500–3000 km for a half-wavelength, with the EIG wave being on the larger end of this scale. Like all of the time-longitude sections of the different wave types, the high-amplitude features appear as somewhat infrequent bursts of convective activity. Components of the red background, that are inevitably included in these filtered datasets, are hidden by our choice to omit the zero contour for these plots.

5. Summary of wave types

Each wave disturbance that has been isolated in the OLR spectra will be summarized to place the results shown here into context with those of previous studies. As this study has looked at the majority of the spectral peaks of tropical convection in the range of planetary to synoptic scales, and from intraseasonal timescales down to a period of 1.25 days, numerous previous studies that have focused on subsets of this wavenumber-frequency domain will be highlighted. For this we concentrate on the convectively coupled equatorial waves. These waves are much less well known and much less previously studied than the MJO or TD-type distur-

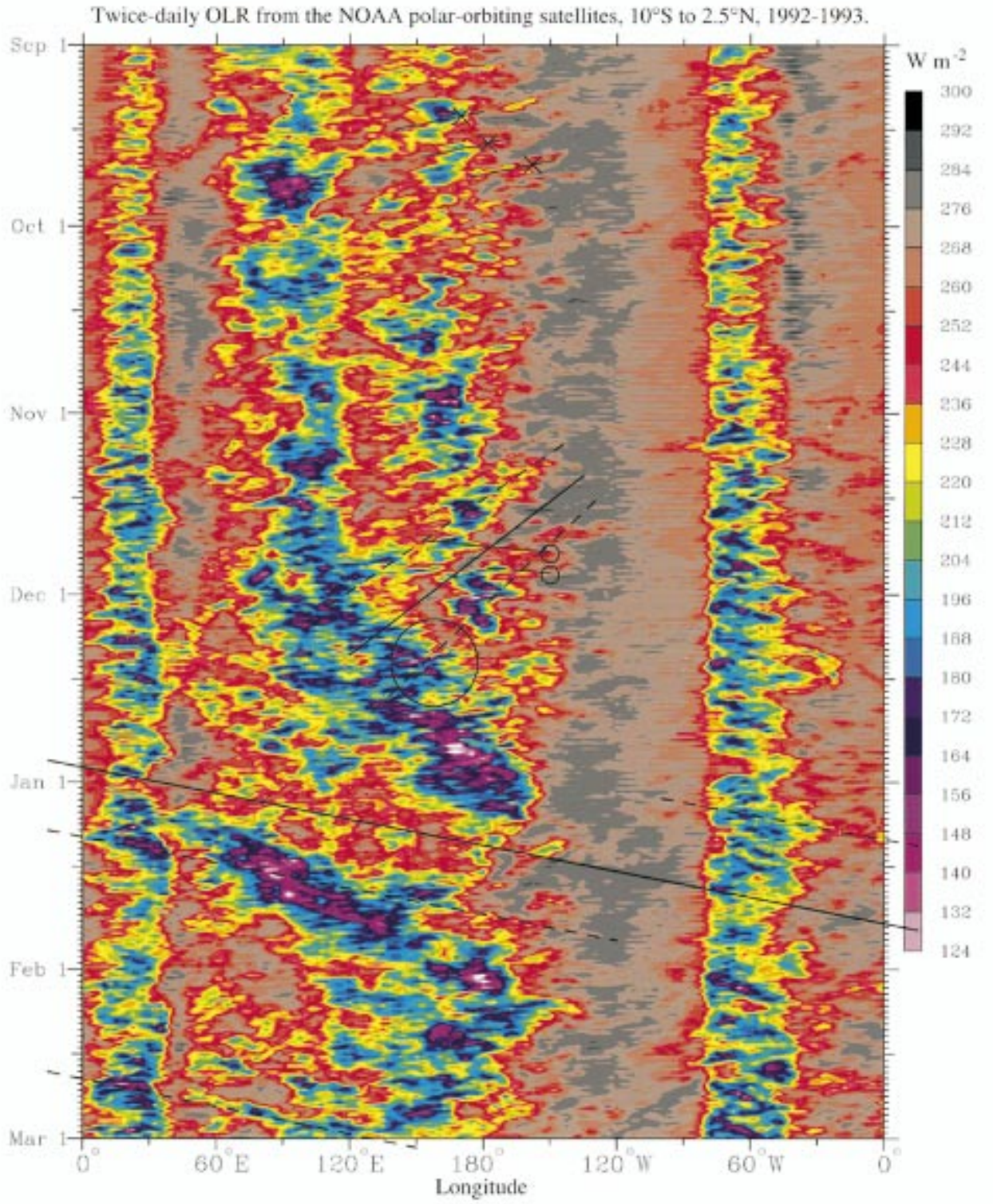

FIG. 8. Time-longitude section of the twice-daily total OLR (W m^{-2}) averaged for the latitudes from 10°S to 2.5°N and for 6 Z 1 September 1992 through 6 Z 1 March 1993. Values correspond to the color bar. Each time section consists of half nighttime and half daytime data from the polar-orbiting satellite (see text for details). Dark lines, circles, and crosses refer to convectively coupled equatorial wave disturbances, and match those of Fig. 9.

bances. These latter two types of disturbances could be classified as convectively coupled, but not simple equatorial waves, due to their location away from the shallow water wave dispersion curves in the wavenumber-frequency domain.

a. Kelvin wave

We have shown that this wave globally explains about the same amount of convective variance as the MJO, yet is quite different to the MJO in many respects. It is faster, occurs over a larger range of wavenumbers and frequencies, is more global in its occurrence in longitude as a convectively coupled signal, and more meridionally confined and centered on the equator. Previous observational studies of disturbances that are similar to what we have called the convectively coupled Kelvin wave are those of Nakazawa (1988), Hayashi and Nakazawa (1989), Takayabu and Murakami (1991), and Dunkerton and Crum (1995). Those studies termed these disturbances ''superclusters,'' although it appears that what is typically thought of as a supercluster moves a little slower than the convectively coupled Kelvin wave disturbances found to be most statistically significant here (10–15 m s^{-1} compared to about 11–22 m s^{-1}). Some of this discrepancy can be explained by the fact that the superclusters of the previous studies were of a wavenumber scale of about 6–15, which, as can be calculated from Fig. 3b, would correspond to a somewhat slower propagation speed. Nakazawa (1986), on the other hand, obtained a typical eastward phase speed of about 18 m s^{-1} for synoptic envelopes of convection within the MJO, much the same as that obtained for the Kelvin modes here.

There have also been several theoretical studies of Kelvin waves. As an example, Chang and Lim (1988) studied the theory of the Kelvin wave-CISK modes on the equatorial β-plane, although they were motivated by an explanation for the MJO, and not the convectively coupled Kelvin waves that we have shown here to be distinctly different to the MJO. This suggests that some of the theoretical studies of the MJO that produce disturbances that are seemingly too fast, might in fact be a more adequate theoretical explanation of the convectively coupled Kelvin waves.

b. $n = 1$ ER wave

Globally, the $n = 1$ ER wave explains somewhat less convective variance than the MJO or the convectively coupled Kelvin wave. In a few off-equatorial regions, however, such as Northern Australia or around the Philippines, this variance is greater than that of the Kelvin wave, and comparable to that of the MJO. It would thus seem that real-time monitoring of the convectively coupled $n = 1$ ER wave could have important implications for extended-range weather prediction in those regions. Kiladis and Wheeler (1995) looked in detail at $n = 1$ ER waves and their links to convection and noted the typical scale of wavenumber 6 and a period around 10–15 days in the Pacific sector. This is in agreement with the scales shown to be of prominence here, although we also point to the predominance of lower wavenumber and lower frequency disturbances that lie along a similar dispersion curve. Kiladis and Wheeler (1995) also estimated the phase speeds of the disturbances across the Pacific to be in the range of 5–10 m s^{-1}, which is a little faster than what we have been shown to be typical here. The reason for this discrepancy likely relates to the fact that here we have concentrated on the deep convective signal, whereas our earlier study concentrated on the circulation features. As we will discuss in the next section, and as evident in the cross-spectra in Fig. 4, an association with convection appears to slow the waves when compared to equivalent dry modes.

c. MRG wave

In terms of the amount of variance explained globally, the convectively coupled MRG wave appears to be the next in importance after the ER wave. This wave type has been the subject of much research. Zangvil (1975), Zangvil and Yanai (1981), Liebmann and Hendon (1990), Hendon and Liebmann (1991), Takayabu and Nitta (1993), and Dunkerton and Baldwin (1995) are among the many studies that have looked at the coupling of convection with MRG waves around the region of the dateline. These papers have also emphasized the distinction between the convectively coupled MRG waves and the TD-type disturbances, with the latter having a similar frequency but being more confined to the western Pacific.

We are also able to show the distinction between the convectively coupled MRG waves and TD-type disturbances within the space-time spectra (Fig. 5). The MRG waves are of lower wavenumber (wavenumbers 1–5) and also only present in the antisymmetric component of OLR. Also of note is the geographical position of the maximum convective signal of the convectively coupled MRG wave to the east of the main center of convection in Figs. 7i and 7j, near the dateline. Hendon and Liebmann (1991) postulated that the waves may be generated in this region due to the unique meridional distribution of SSTs there. Extratropical wave energy as another possible source for MRG disturbances has also been discussed by Magaña and Yanai (1995). Given the eastward group speed of such waves, the existence of the highly varying and strong convective signal of the western Pacific cannot be ruled out as an additional source. A typical scenario for the generation of such waves may be that the mostly red-noise background spectrum of tropical convection intermittently has a strong projection onto the frequency and wavenumber scales of the convectively coupled equatorial waves. Why the particular equivalent depth-scale of the con-

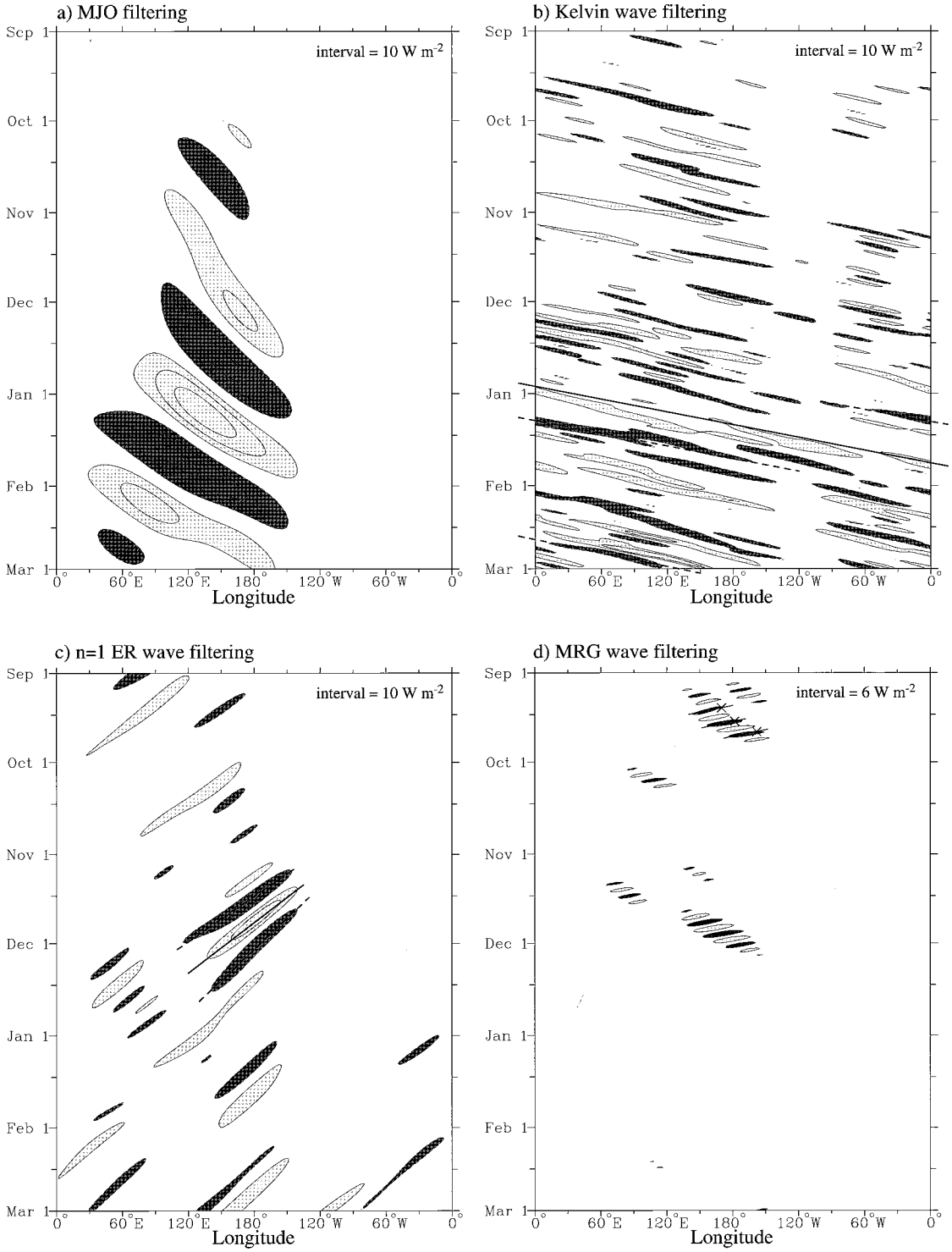

FIG. 9. (a) Time-longitude section of the OLR anomalies for the MJO-filtered band for the same 6-month sample period as Fig. 8, averaged for the latitudes from 10°S to 2.5°N. The zero contour has been omitted. Light shading for positive anomalies and dark shading and dashed contours for negative anomalies. (b) Same as in panel a except for the Kelvin wave–filtered band. (c) The $n = 1$ ER wave–filtered band. (d) The MRG wave–filtered band.

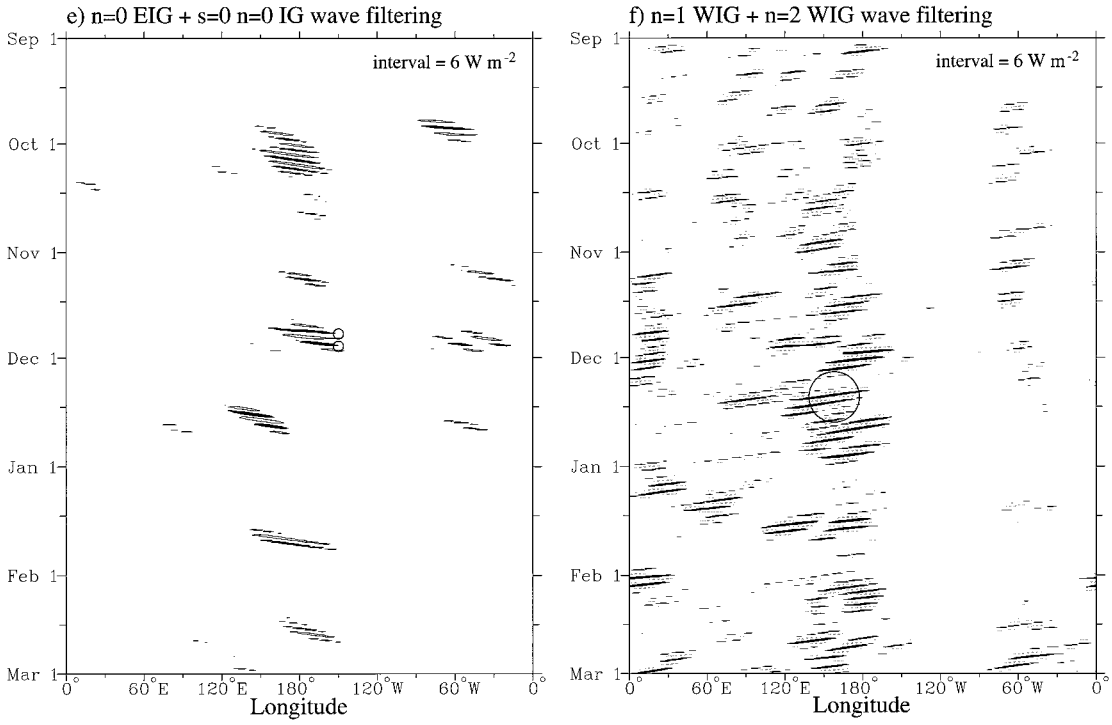

FIG. 9 (*Continued*) (e) The $n = 0$ EIG wave–filtered plus the $s = 0$, $n = 0$ IG wave–filtered band. (f) The $n = 1$ WIG wave–filtered plus the $n = 2$ WIG wave–filtered bands.

vectively coupled waves is chosen is a good topic for future study.

d. n = 0 EIG wave

The convectively coupled $n = 0$ EIG wave explains a similar amount of variance as the convectively coupled MRG wave, and also has a similar geographical distribution. A prominent difference, however, is that it has eastward phase propagation with speeds between about 25–50 m s^{-1}, and it also includes a wider range of spatial scales, with a significant signal extending out to about wavenumber 12. To our knowledge, this convectively coupled wave has not been observed in any detail elsewhere. Of particular interest is the zonal-mean signal of this wave near a period of 4 days.

e. n = 1 and n = 2 WIG waves

These convectively coupled waves together explain the predominance of westward moving organizations of mesoscale convective activity on the 1.25–2.5-day timescale. Such organizations have a spatial scale on the order of 2000 km, and their existence can be seen within the time-longitude plots of Nakazawa (1988), Mapes and Houze (1993), Takayabu (1994b), and Hendon and Liebmann (1994). Like the study of Takayabu (1994b), we find that these westward moving signals in the convection have wavenumber-frequency relations like those of the $n = 1$ and $n = 2$ WIG waves. The scales that have most power are for wavenumbers from around 4 to 14 for the $n = 1$ wave (Fig. 1b) and from wavenumbers 1 to 10 for the $n = 2$ wave (Fig. 1a). The absence of the counterparts of these waves in the eastward moving direction has been hypothesized to be the result of the more complex latitudinal distribution of divergence of the $n = 1$ and $n = 2$ EIG waves (Takayabu 1994b). Indeed, this hypothesis relates back to the work of Lindzen (1974) on wave–CISK in the Tropics, in which he found that the latitudinal distribution of warm and moist conditions favorable for deep convection, combined with the meridional structure of the divergence field of the eastward $n = 1$ and $n = 2$ inertio-gravity waves, made these waves more dynamically stable. The same reasoning may be used to explain the absence of higher meridional mode-numbered inertio-gravity and Rossby waves in the spectra as well, an argument that is independent of the specific choice of convective parameterization.

Also of interest is the correspondence of some of the spectral peaks in tropical convection with some of the observed equatorial waves of the lower stratosphere. The wavenumber 1 and 2 spectral peaks of the convectively coupled Kelvin wave at periods of 20 and 10 days, respectively, (Fig. 3b) are like that found by Wallace and Kousky (1968) in the circulation of the lower stratosphere. Indeed, the wavenumber 1 convectively coupled Kelvin wave during January 1993 (Fig. 9b)

occurred at the same time as a strong Kelvin wave signal of similar frequency in the lower stratosphere (see Gutzler et al. 1994). For the convectively coupled MRG wave, there is statistically significant power at periods of around 4–5 days (Fig. 3a), which coincides quite nicely with the timescale of the lower-stratospheric MRG waves as observed by Yanai and Maruyama (1966) in the circulation. It is likely that the preferred scales of the other convectively coupled equatorial waves should also be reproduced in the lower stratosphere, especially for the faster moving inertio-gravity waves that are less affected by the basic-state zonal winds.

6. Discussion of the equivalent depth

In this paper we have shown that there are spectral peaks in OLR that imply equivalent depths for convectively coupled equatorial waves in the range of 12–50 m (Fig. 3). We have also shown that there are prominent spectral peaks in the dynamical fields alone that occur for deeper equivalent depths of around $h = 200$ m (Figs. 4e,f). The significance of these equivalent depths for the convectively coupled and nonconvectively coupled waves of the troposphere deserves some discussion. Obviously, it will be important to try to distinguish between those waves that are forcing, and those that are forced by deep convection.

As already mentioned, the equivalent depth formally appears as a separation constant linking the vertical structure equation and the shallow water equations (e.g., Lindzen 1967), and is obtained as an eigenvalue for each solution of the vertical structure equation. For stability conditions representative of the tropical troposphere, dry wave motions with a half-wavelength vertical structure extending over the depth of the troposphere, or full vertical wavelength of about $L_z = 28$ km, have equivalent depths of around $h = 200$ m.[2] As h approximately scales with the square of L_z, a vertical wavelength of about 14 km corresponds to an equivalent depth of about 50 m. The relationship between h and L_z also depends upon the static stability, such that L_z is smaller for a given h in regions of high stability (such as the lower stratosphere), or h is smaller for a given L_z in regions of low stability (such as the upper troposphere).

To relate h to the vertical modes forced by the convection, we consider the response of the tropical troposphere to an isolated diabatic convective heating—that is, one that is subsequently turned off. The equatorial wave vertical projection response consists of a continuum of scales centered about vertical wavelengths twice the effective depth of the heating (e.g., Chang 1976; Fulton and Schubert 1985; Salby and Garcia 1987). For deep convective heating extending over a depth of about 14 km (e.g., Frank and McBride 1989), the projection thus gives a vertical wavelength scale centered around $L_z = 28$ km and equivalent depth of around $h = 200$ m. Wave motions with this vertical scale, or a half-wavelength within the troposphere, are generally observed to be the most energetic in the dynamical fields of the tropical troposphere (Silva Dias 1986), and are sometimes referred to as the tropospheric first-baroclinic vertical mode (e.g., Milliff and Madden 1996). We have referred to this vertical mode as the peak projection response to deep convective heating, and it is quite prominent in the spectra of the dynamical fields (e.g., Figs 4e,f). More detailed calculations of the projection response using observed profiles of diabatic heating and static stability (Fulton and Schubert 1985; Mapes and Houze 1995) determine the internal gravity wave speed of the peak projection response to be around 40–50 m s^{-1}, consistent with the equivalent depth of around 200 m considered here. Besides this peak projection response to deep convective heating, however, in recent years it has become increasingly apparent that there is also the more shallow response from the heating profile associated with the stratiform precipitation of older convective cells (e.g., Houze 1982; Hartmann et al. 1984). Mapes and Houze (1995) estimated that the vertical mode produced by this secondary heating profile has a vertical wavelength about half as great, and thus an equivalent depth one-quarter as large.

A further issue concerns the mechanism that determines the equivalent depth of the equatorial waves associated with deep convection. The present study, like previous observational studies (e.g., Liebmann and Hendon 1990; Takayabu 1994a), has shown that the equivalent depth linked with the large-scale convective disturbances of the Tropics is much smaller than the equivalent depth of the peak projection response. There are two main schools of thought of why this may be so. One is that the latent heat release occurs in regions of upward motion, which compensates the reduction in perturbation temperature due to lifting, and thus effectively reduces the static stability, slowing the waves (e.g., Gill 1982; Emanuel et al. 1994). The other is that the shallower, but less energetic, vertical mode of stratiform precipitation, as shown to exist in the observations of Mapes and Houze (1995), is more important for providing the environment for subsequent convection to occur (see also Lindzen 1974; Stevens et al. 1977; Mapes 1997). Such a shallower mode would have a smaller equivalent depth and be associated with slower phase speeds. Of course, diabatic heating within precipitating deep convection is an inherently nonlinear process as there is no equivalent negative heating (e.g., Lau and Peng 1987). Also, within the heating region the vertical scale of the response should resemble that of the heating

[2] This calculation was made for an atmosphere with a constant lapse rate of $dT/dz = -7$ K km^{-1} and mean temperature of 250 K. See Holton (1970) for the appropriate equation in a constant lapse rate atmosphere, and Fulton and Schubert (1985) for calculations in an atmosphere of arbitrary lapse rate.

itself (e.g., Salby and Garcia 1987), and it becomes possible for a coalescence of two internal vertical modes to produce slow-moving disturbances (e.g., Chang and Lim 1988).

Ultimately, it is important to know which convectively coupled wave disturbances are important in the real world, and for what wavenumbers and frequencies they are prominent. As opposed to the free (dry) disturbances shown to exist in the dynamics alone, such convectively coupled waves are generally not well simulated in general circulation models, presumably due to the importance of and sensitivity to the cumulus parameterization. We believe that further detailed study of the convectively coupled equatorial waves will provide new insight into the large-scale moist dynamics of the tropical troposphere.

7. Conclusions

Wavenumber-frequency spectral analysis of satellite-observed OLR shows the broad nature of the spectrum of deep tropical convection to be red in both wavenumber and frequency, but with some distinct spectral peaks. Removing an estimated red background spectrum reveals that some of these spectral peaks correspond quite well with the dispersion relations of the equatorially trapped wave modes of shallow water theory. These so-called convectively coupled equatorial waves have a common equivalent depth of around 12–50 m, which is thought to be a result of how the convection is interacting with the dynamics. In the dynamical fields there are also prominent signatures of equatorial waves that correspond to deeper equivalent depths of around $h = 200$ m. These presumably nonconvectively coupled waves can be explained to be a result of the peak projection response to deep convective heating. The convectively coupled equatorial waves we have isolated are the Kelvin, $n = 1$ equatorial Rossby (ER), mixed Rossby-gravity (MRG), $n = 0$ eastward inertio-gravity (EIG), ($n = 1$) westward inertio-gravity (WIG), and $n = 2$ WIG waves. The Madden–Julian oscillation (MJO) and the tropical depression-type (TD-type) disturbances are also present in the spectra.

Some of the wave types corresponding to peaks in the OLR wavenumber-frequency spectra have been studied in detail by other researchers. It is also the case that some of the wave types mentioned here have received little attention in the past, most notably the convectively coupled $n = 1$ ER wave, and three different convectively coupled inertio-gravity waves. This paper attempts to put all of the wave types that can be identified in the OLR field into perspective with each other, and with the seemingly random and nonperiodic variations of deep convection that contribute to the red-noise background spectrum.

Compared to the MJO, the convectively coupled Kelvin wave is faster, more global in its occurrence as a convectively coupled signal, and more confined to the equator. The convectively coupled ER wave has its maximum variance off the equator in the region of the Indian Ocean to the western Pacific Ocean, whereas both the MRG and $n = 0$ EIG waves are shown to be maximized around the region of the dateline. Each convectively coupled wave can also be identified in the total OLR field at some stage during a sample 6-month period of the record.

A typical scenario for the generation of convectively coupled equatorial waves, in addition to that of extratropical forcing (e.g., Magaña and Yanai 1995; Kiladis 1998), may be that the mostly red-noise background spectrum of tropical convection intermittently has a strong projection onto the frequency and wavenumber scales of the convectively coupled equatorial waves. As these scales are the most optimal for an association between the dynamics and tropical convection, the projection produces a packet of the convectively coupled equatorial waves that can further interact with the convection. It would seem likely that the convectively coupled equatorial waves, once generated, are inherently more predictable than weather variations that produce the red-noise background. Extended-range prediction of weather in the Tropics may benefit by consideration of these waves. For example, predictions of weekly weather trends around tropical Australia and Indonesia already rely on information about the phase of the MJO.

It is also hoped that this study will provide further insight toward answering the question of why large-scale variations of deep convection occur when and where they do. This question is quite relevant to the so-called closure problem of cumulus parameterization. It is shown here that an equivalent depth on the order of 25 m is the most optimal for an association of equatorially trapped waves with convection. This is not to say that all equatorially trapped waves within the tropical troposphere should have phase speeds and scales that would match such an equivalent depth. Waves that are not associated with convection are theoretically able to match any equivalent depth scale depending on their vertical structure. The nature of the interaction between convection and dynamics is of crucial importance to the theory and modeling of the tropical atmosphere. It is noteworthy that wavenumber-frequency spectra calculated for a GCM precipitation field by Hayashi and Golder (1994) show little evidence of the convectively coupled equatorial waves.

Finally, the correspondence of some of the strongest statistically significant disturbances in the convection, as shown here, with the wavenumber and frequency characteristics of some of the observed waves of the lower stratosphere is of great interest. Work is in progress to calculate the structure of the circulations associated with each of the statistically significant disturbances.

Acknowledgments. Thanks to Murry Salby, Peter Webster, Klaus Weickmann, Rolando Garcia, Gilbert

Compo, Christopher Torrence, Jeff Hicke, Adrian Matthews, Brian Mapes, Jeff Forbes, and Andrew Moore for helpful discussions throughout the course of this work. We also thank Murry Salby, Richard Lindzen, Yoshikazu Hayashi, Ralph Milliff, and two anonymous reviewers for their detailed comments on the first draft of this paper. The original twice-daily OLR data was obtained from Brant Liebmann and Cathy Smith at the NOAA Climate Diagnostics Center (CDC). The MSU and NCEP/NCAR 40-Year Reanalysis data were also obtained from CDC through their data archives (http://www.cdc.noaa.gov). This research was supported by the TOGA COARE program, funded jointly by NOAA's Office of Global Programs and the National Science Foundation, under project Grant ATM 95-25860. Matthew Wheeler was also supported by a Cooperative Institute for Research in the Environmental Sciences (CIRES) Graduate Research Fellowship at the University of Colorado.

REFERENCES

Amos, D. E., and L. H. Koopmans, 1963: *Tables of the Distribution of the Coefficient of Coherence for Stationary Bivariate Gaussian Processes. Monogr.,* No. SCR-483, Sandia Corp., 325 pp.

Arkin, P. A., and P. E. Ardanuy, 1989: Estimating climatic-scale precipitation from space: A review. *J. Climate,* **2,** 1229–1238.

Bantzer, C. H., and J. M. Wallace, 1996: Intraseasonal variability in tropical mean temperature and precipitation and their relation to the tropical 40–50 day oscillation. *J. Atmos. Sci.,* **53,** 3032–3045.

Bergman, J. W., and M. L. Salby, 1994: Equatorial wave activity derived from fluctuations in observed convection. *J. Atmos. Sci.,* **51,** 3791–3806.

Chang, C. P., 1970: Westward propagating cloud patterns in the tropical Pacific as seen from time composite satellite photographs. *J. Atmos. Sci.,* **27,** 133–138.

——, 1976: Forcing of stratospheric Kelvin waves by tropospheric heat sources. *J. Atmos. Sci.,* **33,** 740–744.

——, and H. Lim, 1988: Kelvin-wave CISK: A possible mechanism for the 30–50 day oscillations. *J. Atmos. Sci.,* **45,** 1709–1720.

Chen, S. S., R. A. Houze., and B. E. Mapes, 1996: Multiscale variability of deep convection in relation to large-scale circulation in TOGA COARE. *J. Atmos. Sci.,* **53,** 1380–1409.

Dunkerton, T. J., and M. P. Baldwin, 1995: Observation of 3–6 day meridional wind oscillations over the Tropical Pacific, 1973–1992: Horizontal structure and propagation. *J. Atmos. Sci.,* **52,** 1585–1601.

——, and F. X. Crum, 1995: Eastward propagating ~2- to 15-day equatorial convection and its relation to the tropical intraseasonal oscillation. *J. Geophys. Res.,* **100,** 25 781–25 790.

Emanuel, K. A., J. D. Neelin, and C. S. Bretherton, 1994: On large-scale circulations in convecting atmospheres. *Quart. J. Roy. Meteor. Soc.,* **120,** 1111–1143.

Frank, W. M., and J. L. McBride, 1989: The vertical distribution of heating in AMEX and GATE cloud clusters. *J. Atmos. Sci.,* **46,** 3464–3478.

Fulton, S. R., and W. H. Schubert, 1985: Vertical normal mode transforms: Theory and application. *Mon. Wea. Rev.,* **113,** 647–658.

Garcia, R. R., and M. L. Salby, 1987: Transient response to localized episodic heating in the Tropics. Part II. Far-field behavior. *J. Atmos. Sci.,* **44,** 499–530.

Gill, A. E., 1982: Studies of moisture effects in simple atmospheric models: The stable case. *Geophys. Astrophys. Fluid Dyn.,* **19,** 119–152.

Gruber, A., 1974: The wavenumber-frequency spectra of satellite-measured brightness in the Tropics. *J. Atmos. Sci.,* **31,** 1675–1680.

——, and A. F. Krueger, 1984: The status of the NOAA outgoing longwave radiation data set. *Bull. Amer. Meteor. Soc.,* **65,** 958–962.

Gutzler, D. S., G. N. Kiladis, G. A. Meehl, K. M. Weickmann, and M. Wheeler: 1994: The global climate of December 1992–February 1993. Part II: Large-scale variability across the tropical western Pacific during TOGA COARE. *J. Climate,* **7,** 1606–1622.

Hartmann, D. L., H. H. Hendon, and R. A. Houze, 1984: Some implications of the mesoscale circulations in tropical cloud clusters for large-scale dynamics and climate. *J. Atmos. Sci.,* **41,** 113–121.

Hayashi, Y., 1982: Space-time spectral analysis and its applications to atmospheric waves. *J. Meteor. Soc. Japan,* **60,** 156–171.

——, and T. Nakazawa, 1989: Evidence of the existence and eastward motion of superclusters at the equator. *Mon. Wea. Rev.,* **117,** 236–243.

——, and D. G. Golder, 1994: Kelvin and mixed Rossby–gravity waves appearing in the GFDL ''SKYHI'' general circulation model and the FGGE dataset: Implications for their generation mechanism and role in the QBO. *J. Meteor. Soc. Japan,* **72,** 901–935.

——, and ——, 1997: United mechanisms for the generation of low- and high-frequency tropical waves. Part I: Control experiments with moist convective adjustment. *J. Atmos. Sci.,* **54,** 1262–1276.

Hendon, H. H., and B. Liebmann, 1991: The structure and annual variation of antisymmetric fluctuations of tropical convection and their association with Rossby–gravity waves. *J. Atmos. Sci.,* **48,** 2127–2140.

——, and ——, 1994: Organization of convection within the Madden-Julian oscillation. *J. Geophys. Res.,* **99,** 8073–8083.

Hess, P., H. H. Hendon, and D. S. Battisti, 1993: The relationship between mixed Rossby–gravity waves and convection in a general circulation model. *J. Meteor. Soc. Japan,* **71,** 321–338.

Holton, J. R., 1970: A note on forced equatorial waves. *Mon. Wea. Rev.,* **98,** 614–615.

——, 1972: Waves in the equatorial stratosphere generated by tropospheric heat sources. *J. Atmos. Sci.,* **29,** 368–375.

Houze, R. A., 1982: Cloud clusters and large-scale vertical motions in the Tropics. *J. Meteor. Soc. Japan,* **60,** 396–410.

Kalnay, E., and Coauthors, 1996: The NCEP/NCAR 40-Year Reanalysis Project. *Bull. Amer. Meteor. Soc.,* **77,** 437–471.

Kiladis, G. N., 1998: Observations of Rossby waves linked to convection over the eastern tropical Pacific. *J. Atmos. Sci.,* **55,** 321–339.

——, and M. Wheeler, 1995: Horizontal and vertical structure of observed tropospheric equatorial Rossby waves. *J. Geophys. Res.,* **100** (D11), 22 981–22 997.

Lau, K.-M., and L. Peng, 1987: Origin of low frequency (intraseasonal) oscillations in the tropical atmosphere. Part I: Basic theory. *J. Atmos. Sci.,* **44,** 950–972.

——, and P. H. Chan, 1988: Intraseasonal and interannual variations of tropical convection: A possible link between the 40–50 day oscillation and ENSO? *J. Atmos. Sci.,* **45,** 506–521.

Liebmann, B., and H. H. Hendon, 1990: Synoptic-scale disturbances near the equator. *J. Atmos. Sci.,* **47,** 1463–1479.

——, and C. A. Smith, 1996: Description of a complete (interpolated) outgoing longwave radiation dataset. *Bull. Amer. Meteor. Soc.,* **77,** 1275–1277.

Lin, X., and R. H. Johnson, 1996: Kinematic and thermodynamic characteristics of the flow over the western Pacific warm pool during TOGA COARE. *J. Atmos. Sci.,* **53,** 695–715.

Lindzen, R. S., 1967: Planetary waves on beta planes. *Mon. Wea. Rev.,* **95,** 441–451.

——, 1974: Wave-CISK in the Tropics. *J. Atmos. Sci.,* **31,** 156–179.

——, and J. R. Holton, 1968: A theory of the quasi-biennial oscillation. *J. Atmos. Sci.,* **25,** 1095–1107.

Madden, R., and P. Julian, 1994: Observations of the 40–50-day tropical oscillation—A review. *Mon. Wea. Rev.,* **122,** 814–837.

Magaña, V., and M. Yanai, 1995: Mixed Rossby–gravity waves triggered by lateral forcing. *J. Atmos. Sci.,* **52,** 1473–1486.

Mapes, B. E., 1997: Equilibrium versus activation control of large-scale variations of tropical deep convection. *The Physics and Parameterization of Moist Convection,* R. K. Smith, Ed., Kluwer Academic, 512 pp.

——, and R. A. Houze, 1993: Cloud clusters and superclusters over the oceanic warm pool. *Mon. Wea. Rev.,* **121,** 1398–1415.

——, and ——, 1995: Diabatic divergence profiles in western Pacific mesoscale convective systems. *J. Atmos. Sci.,* **52,** 1807–1828.

Matsuno, T., 1966: Quasi-geostrophic motions in the equatorial area. *J. Meteor. Soc. Japan,* **44,** 25–43.

Meehl, G. A., 1987: The annual cycle and interannual variability in the tropical Pacific and Indian Ocean regions. *Mon. Wea. Rev.,* **115,** 27–50.

Milliff, R. F., and R. A. Madden, 1996: The existence and vertical structure of fast, eastward-moving disturbances in the equatorial troposphere. *J. Atmos. Sci.,* **53,** 586–597.

Nakazawa, T., 1986: Mean features of 30–60 day variations as inferred from 8-year OLR data. *J. Meteor. Soc. Japan,* **64,** 777–786.

——, 1988: Tropical super clusters within intraseasonal variations over the western Pacific. *J. Meteor. Soc. Japan,* **66,** 823–839.

Salby, M. L., and R. R. Garcia, 1987: Transient response to localized episodic heating in the Tropics. Part I: Excitation and short-time near field behavior. *J. Atmos. Sci.,* **44,** 458–498.

——, and H. H. Hendon, 1994: Intraseasonal behavior of clouds, temperature, and motion in the Tropics. *J. Atmos. Sci.,* **51,** 2207–2224.

Silva Dias, P. L., 1986: Vertical mode decomposition and model resolution. *Tellus,* **38A,** 205–214.

Spencer, R. W., J. R. Christy, and N. C. Grody, 1990: Global atmospheric temperature monitoring with satellite microwave measurements: Method and results 1979–84. *J. Climate,* **3,** 1111–1128.

Stevens, D. E., R. S. Lindzen, and L. J. Shapiro, 1977: A new model of tropical waves incorporating momentum mixing by cumulus convection. *Dyn. Atmos. Oceans,* **1,** 365–425.

Takayabu, Y. N., 1994a: Large-scale cloud disturbances associated with equatorial waves. Part I: Spectral features of the cloud disturbances. *J. Meteor. Soc. Japan,* **72,** 433–448.

——, 1994b: Large-scale cloud disturbances associated with equatorial waves. Part II: Westward propagating inertio-gravity waves. *J. Meteor. Soc. Japan,* **72,** 451–465.

——, and M. Murakami, 1991: The structure of super cloud clusters observed on 1–20 June 1986 and their relationship to easterly waves. *J. Meteor. Soc. Japan,* **69,** 105–125.

——, and T. Nitta, 1993: 3–5 day period disturbances coupled with convection over the tropical Pacific Ocean. *J. Meteor. Soc. Japan,* **71,** 221–246.

Wallace, J. M., and V. E. Kousky, 1968: Observational evidence of Kelvin waves in the tropical stratosphere. *J. Atmos. Sci.,* **25,** 280–292.

Webster, P. J., and R. Lukas, 1992: TOGA COARE: The coupled ocean–atmosphere response experiment. *Bull. Amer. Meteor. Soc.,* **73,** 1377–1416.

Weickmann, K. M., and S. J. S. Khalsa, 1990: The shift of convection from the Indian Ocean to the western Pacific Ocean during a 30–60-day oscillation. *Mon. Wea. Rev.,* **118,** 964–978.

Xie, X., and B. Wang, 1996: Low-frequency equatorial waves in vertically sheared zonal flow. Part II: Unstable waves. *J. Atmos. Sci.,* **53,** 3589–3605.

Yanai, M., and T. Maruyama, 1966: Stratospheric wave disturbances propagating over the equatorial Pacific. *J. Meteor. Soc. Japan,* **44,** 291–294.

Zangvil, A., 1975: Temporal and spatial behavior of large-scale disturbances in tropical cloudiness deduced from satellite brightness data. *Mon. Wea. Rev.,* **103,** 904–920.

——, and M. Yanai, 1981: Upper tropospheric waves in the Tropics. Part II: Association with clouds in the wavenumber-frequency domain. *J. Atmos. Sci.,* **38,** 939–953.

Zhang, C., and P. J. Webster, 1989: Effects of zonal flows on equatorially trapped waves. *J. Atmos. Sci.,* **46,** 3632–3652.

Zhang, M., and M. A. Geller, 1994: Selective excitation of tropical atmospheric waves in wave-CISK: The effect of vertical shear. *J. Atmos. Sci.,* **51,** 353–368.